2017

Status Monitoring Of Inflatables By Accurate Shape Sensing

Justin Matthew Bond
University of Vermont

STATUS MONITORING OF INFLATABLES BY ACCURATE SHAPE SENSING

A Thesis Presented

by

Justin M. Bond

to

The Faculty of the Graduate College

of

The University of Vermont

In Partial Fulfillment of the Requirements
for the Degree of Master of Science
Specializing in Mechanical Engineering

January, 2017

Defense Date: November 7, 2016
Thesis Examination Committee:

Dryver R. Huston, Ph.D., Advisor
Ehsan Ghazanfari, Ph.D., Chairperson
Rachael Oldinski, Ph.D.
Cynthia J. Forehand, Ph.D., Dean of the Graduate College

ABSTRACT

The use of inflatable structures in aerospace applications is becoming increasingly widespread. In order to monitor the inflation status and overall health of these inflatables, an accurate means of shape sensing is required. To this end, we investigated two existing methods for measuring simple curvature, or curvature in one-dimension. The first method utilizes a pair of strain sensing Fiber Bragg Gratings (FBGs) separated by a known distance; dividing the difference in strain by the separation distance yields an experimental value for the one-dimensional curvature at a point. The second method makes use of conductive ink-based flex sensors, which give a variable resistance based on curvature. We used the latter was in a design for a Curvature-Based Inflation Controller (CBIC). While the controller successfully inflated a test body, its overall utility is limited by the simplicity of its sensors. To improve the shape sensing capabilities of the controller, we investigated the use of FBGs in a multidimensional array.

We fabricated a curvature-sensing FBG pair on an inflatable membrane and tested its accuracy as the membrane was shaped into a known radius of curvature. This work reports on the assembly of three such curvature-sensing FBG pairs into a two-dimensional Curvature-Sensing Rosette (CSR). The goal is to use this rosette to measure the curvature of a surface in multiple directions at a single point. A 3-D printed surface with saddle geometry was used to calibrate the curvature-sensing rosette. Presented will be methods of extracting values for the tensor of curvature for the surface at a point using the curvature-sensing rosette, along with experimental verification. This essentially defines the local geometry about the rosette, measured in real time. By employing an array of such rosettes across the surface of an inflatable structure, the local curvature of the inflatable could be known at every point. Combining these curvature measurements can yield an accurate depiction of the global geometry. Thus, the inflation status of the inflatable space structure could be monitored in real time.

TABLE OF CONTENTS

Page

LIST OF TABLES

Table Page

LIST OF FIGURES

CHAPTER 1: INTRODUCTION

The field of space exploration has experienced significant growth in recent years. Technological advances in the industry have nearly eliminated some of the barriers traditionally associated with studying the cosmos. One of the most notable breakthroughs has been the use of inflatable structures in space. The earliest inflatables were large reflector dishes for antennae, and presented several inherent advantages over their rigid metal counterparts [1]. For example, an inflatable space antenna reflector would naturally weigh less, and could be stowed, uninflated, throughout the launching process. The inflatable antenna could then easily survive the violent conditions of takeoff, which would otherwise pose a quandary. In order to withstand the dynamics of a launch, most structures intended for use in space would need to be separated into several smaller components, and each of these would require its own launch vehicle, mission, etc. By employing inflatable reflectors, however, researchers could send a probe with a compact antenna package into space and then expand the inflatable reflector to be much larger than the vessel which originally carried it. NASA's Inflatable Antenna Experiment of 1996 shows this in the figure below (Figure 1).

Figure 1: NASA Inflatable Antenna Experiment [2]

In the image above, the large silver reflector surface and the three beams connecting to it were inflated after launch; the takeoff vessel only needed to be large enough to carry the small copper-colored satellite. These inflatable antenna reflectors were first tested in the 1990s, and many are used to this day for the convenient advantages they provide.

More recently, inflatables have been tested for use in space applications as aerodynamic decelerators and structural sections of space stations. NASA's Hypersonic Inflatable Aerodynamic Decelerator (HIAD) is showing promise as the next-generation solution for atmospheric entry, and presents many attractive qualities over traditional decelerators [3]. Just as the antenna reflector, an inflatable aerodynamic decelerator can be stored for the takeoff and flight portions of a mission, then deploy for atmospheric entry. The HIAD system developed by NASA can be seen in the figure below (Figure 2).

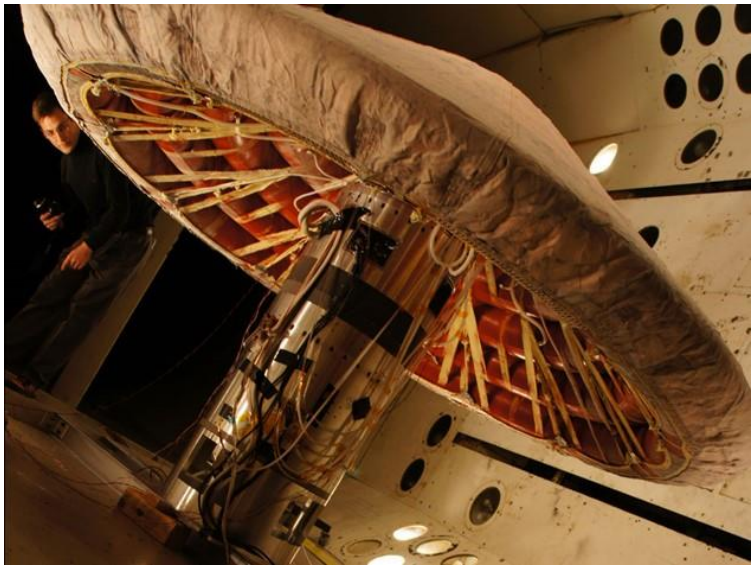

Figure 2: NASA Hypersonic Inflatable Aerodynamic Decelerator [4]

Beneath the grey heat-resistant fabric, there are several inflatable torus-like bodies, or toroids. These concentric rings give the HIAD system its shape and structure, with many reinforcing straps to improve rigidity. Again, this decelerator can inflate to be larger than the landing vehicle, which is extremely beneficial to its utility. In fact, such an inflatable would be critical to the objectives of the mission. Indeed, any mission involving an inflatable structure would depend highly on the successful deployment of that inflatable structure. Thus, obtaining an accurate depiction of the inflation process is particularly important to the industry. It would allow mission controllers to monitor the status of the inflatable and make vital decisions about the current mission.

Monitoring the progress of an inflating structure can be essential, but performing such a task in space is inherently nontrivial. For instance, much of the inflating is controlled remotely and without any visual cues present. Current methods of controlling

inflation utilize pressure measurements within the inflatable to determine the progress of the inflation, but pressure readings alone are insufficient for assessing the process itself. Such methods depend upon the inflation process to be smooth and without complication. Were an issue to arise, such as unexpected entanglement of the uninflated body, a simple pressure measurement would not identify the problem. In fact, the inflation process would likely continue unabated, potentially causing catastrophic damage to the inflatable and surrounding hardware. Given the nature of these missions, such a failure to diagnose an inflation problem would certainly result in significant financial loss, in addition to months of planning being wasted. Clearly, a more comprehensive method of monitoring inflation is required.

In the absence of direct visual confirmation, a means of inferring the overall shape and status of an inflatable could provide the feedback necessary to safely deploy an inflatable. This is known as shape sensing, which is a method for detecting the geometry of an inflatable body. Shape sensing utilizes sensors placed about the inflatable to monitor the inflation status in real time. Because this method allows one to observe the geometry of the body, any issues that might prevent the inflatable from successfully deploying would be instantly identified. Moreover, once the structure was completely inflated, an accurate shape sensing system would provide a means of health monitoring. For instance, any minor deflection of a surface on the body due to debris impact or structural anomaly would be quickly detected. Shape sensing can greatly reduce the risks associated with deploying inflatable structures, which is why there have been significant efforts to investigate practical methods of sensing shape.

One such effort has been made recently by researchers at NASA, led by Jason P. Moore [5]. Using a chain of connected fiber optic strain gauges, called Fiber Bragg Gratings (FBGs), they have developed a cable which measures curvature at numerous points along its length. Curvature is a vector quantity that describes the degree and direction to which an arc is curved. Mathematically, curvature is the inverse of the Radius of Curvature, which is just the instantaneous radius required to produce the curve at a particular point [6]. Engineers like Jason P. Moore are interested in measuring curvature for its relationship to shape sensing: if the curvature of a body is known at a point, then the local geometry about that point can be inferred. In order to fully specify the curvature of a surface, three separate components must be measured. Assuming the curvature can be found at many points about the body, the complete geometry of the inflatable can be known. Or, by taking curvature measurements at specific points on the body, the inflation status and shape can be monitored and controlled.

In the first portion of this investigation, a design for a novel inflation controller is presented. Rather than relying on internal pressure readings, this device uses simple bend sensors to detect the curvature at several points on the inflatable body. By using these curvature readings as feedback, the Curvature-Based Inflation Controller (CBIC) is able to successfully inflate an object to a desired level. Despite using a unique measure for its feedback, this controller still suffers many of the pitfalls associated with traditional pressure-based controllers. Chief among them is the necessity for the inflation process itself to be spatially smooth and gradual. This is due to the nature of the curvature sensors that were used; they can only measure simple curvature, or curvature in one direction. This

means that the final inflated geometry must be known, and all of the sensor data are merely compared to the desired final values for curvature. The controller and sensor configuration would thus need to be altered for every new inflatable geometry. In order to improve the reliability and utility of the inflation controller, the sensors themselves would need to become more sophisticated.

The NASA FBG chain is a powerful sensing system, capable of giving the operator a clear view of the shape of the cable itself. However, just as the bend sensors used in the CBIC, this fiber optic sensor bundle will only give the one-dimensional curvature at any point. This is because the NASA cable is in essence a space curve. Space curves are one-dimensional entities that exist in three-dimensional space [6]. The curvature sensing FBG chain can be seen in the figure below (Figure 3).

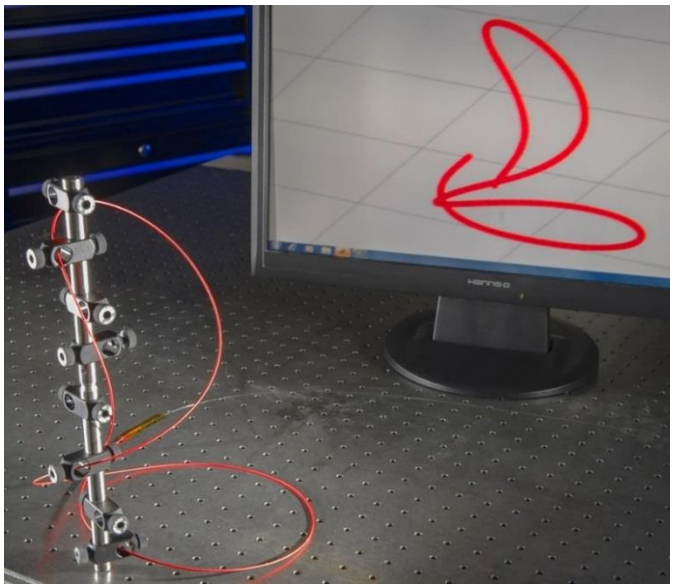

Figure 3: NASA Curvature Sensing Cable [7]

The image above clearly shows the fiber optic cable in the lower left, and the computer generated image of the cable's shape on the monitor in the upper right. Because it is one-

dimensional, the curvature of such a space curve can only occur in one direction at a time. This means that the NASA cable can only measure curvature in a single direction at a time. The surface of an inflatable is a two dimensional body which exists in three-dimensions. In order to completely define the geometry of a surface, additional curvature measurements are required. In fact, the NASA cable is only able to provide an estimate of a surface's geometry when the FBG chain is run across the surface multiple times. The computer-generated image then shows the path of the cable, with minor deflections, often due to twist within the cable itself. While impressive, it is far from being capable of accurately depicting the geometry of a two-dimensional surface. For this, a new type of curvature sensor is required: one which can measure curvature in more than one direction at the same time.

The second portion of this investigation was to design a sensor which could accurately sense the shape of a surface by detecting curvature in more than one direction. This new sensor would necessarily be an array of sensors which could each sense curvature in a single direction. Fiber optic strain gauges were chosen for their high accuracy and proven track record in the NASA FBG chain device, along with their small diameter and sensing footprint geometry. A single pair of FBGs was combined into a curvature sensor, and preliminary tests were performed. Once the method had been refined and results were reliably accurate, an array of three curvature sensors was fabricated. The sensors were placed in a classic strain rosette configuration; the two outer sensors were orthogonal to each other, and the central sensor was aligned with the 45^{o} angle between the other two. In order to calibrate this new curvature sensor array, a custom saddle curve was designed

and 3-D printed. Male and female saddle profiles were fabricated to ensure the sensor array would conform to the test surface of the saddle curve. Testing of this sensor array proved successful; the new curvature sensor accurately detected the two-dimensional curvature of the test surface. Such an array could be extremely useful in sensing the shape of a surface, particularly that of an inflatable space structure. By placing these new sensors at strategic points about an inflatable, the total geometry of the body could be known in real time. Thus, the inflation status and overall health of an inflatable could be monitored as necessary for mission success.

In the next chapter, the task of sensing curvature in one direction will be explored. The mathematical definition of a space curve, as well as some contemporary methods for detecting curvature will be discussed. Chapter 2 concludes with an in-depth analysis of the inflation controller design and utility.

The third chapter examines the task of two-dimensional curvature detection and its challenges. The properties of a surface will be defined mathematically. Finally, the novel method of sensing curvature in multiple directions and its implications will be discussed.

CHAPTER 2: CURVATURE IN ONE DIRECTION

2.1. The Geometry of a Space Curve

In the context of shape sensing, detecting curvature on an inflatable surface is essential. In order to discuss the various methods involved with sensing curvature, it is necessary to fully define curvature as it applies to this topic. In this section, simple or one-dimensional curvature will be discussed. This will involve delineation of the mathematical quantity that is curvature as well as its significance in the real, physical world. As simple curvature is primarily a property of space curves, the definition of a space curve will now be presented.

A space curve is a continuous set of points existing in three-dimensional space [8]. Imagine a very thin wire that curves or bends through different angles and in different directions, such that it cannot be confined to a plane. Although the wire itself has only one dimension of significance, length, it still exists in three-dimensional space. This is, in essence, the physical analog to the mathematical definition of a space curve. Now, let *C* be a particular space curve in which we are interested. Assuming a Cartesian coordinate system is present, then each point on *C* is defined by its position vector [8, 9]. This position vector is denoted as $\boldsymbol{x}$. The vector $\boldsymbol{x}$ has components in the $\boldsymbol{x}_1$, $\boldsymbol{x}_2$, and $\boldsymbol{x}_3$ directions. The following equation shows this [5].

$$\boldsymbol{x}(u) = x_1(u)\boldsymbol{e}_1 + x_2(u)\boldsymbol{e}_2 + x_3(u)\boldsymbol{e}_3 \tag{1}$$

The terms $\boldsymbol{e}_1$, $\boldsymbol{e}_2$, and $\boldsymbol{e}_3$ are the unit normal vectors in the $\boldsymbol{x}_1$, $\boldsymbol{x}_2$, and $\boldsymbol{x}_3$ directions, respectively. Note that $\boldsymbol{x}$ and its components are all functions of the parameter u. This can signify time, but not necessarily so; u is simply a real variable associated with increasing arc length along *C* [8]. The arc length along *C* will now be referred to as s. The parameter s has units of length and increases as u increases. Refer to the following figure for a visual representation of a space curve (Figure 4).

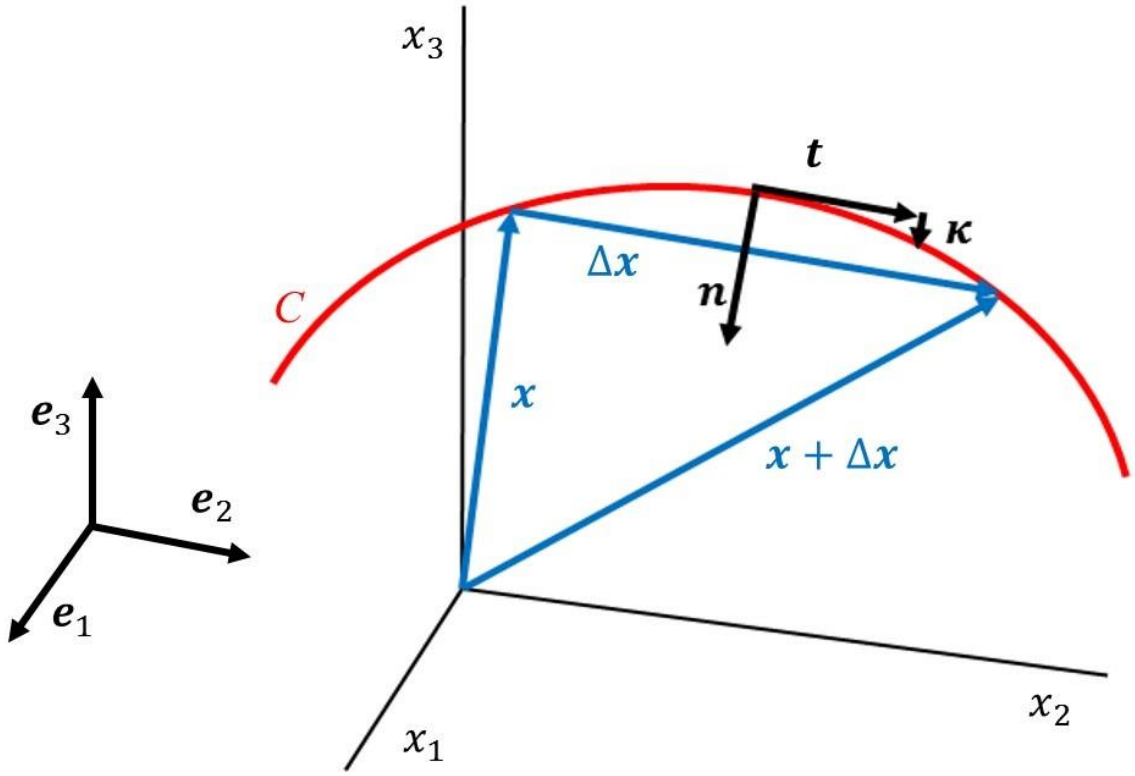

Figure 4: Geometry of a Space Curve

In the figure above, the curved red line represents the space curve, *C*. The position vector $\boldsymbol{x}$ points from the origin to the curve, and s increases along *C* from left to right in the figure. The vector $\Delta\boldsymbol{x}$ illustrates a change in position along *C* as u increases, as if one were

traveling along the curve *C*. The following equation shows the change in $\boldsymbol{x}$ and its components with respect to a change in u:

$$\frac{\Delta \boldsymbol{x}}{\Delta u} = \frac{\Delta x_1}{\Delta u}\boldsymbol{e}_1 + \frac{\Delta x_2}{\Delta u}\boldsymbol{e}_2 + \frac{\Delta x_3}{\Delta u}\boldsymbol{e}_3 \tag{2}$$

Now, taking the limit of the above equation as Δu goes to zero yields the following differential representation of a changing position vector along *C* with respect to u:

$$\frac{d\boldsymbol{x}}{du} = \frac{dx_1}{du}\boldsymbol{e}_1 + \frac{dx_2}{du}\boldsymbol{e}_2 + \frac{dx_3}{du}\boldsymbol{e}_3 \tag{3}$$

The above quantity, $d\boldsymbol{x}/du$, can be thought of as the average velocity of a body moving along *C*. Although it does not explicitly depend on the arc length s, it can be rewritten as follows:

$$\frac{d\boldsymbol{x}}{du} = \frac{d\boldsymbol{x}}{ds}\frac{ds}{du} = \boldsymbol{t}\frac{ds}{du} \tag{4}$$

Here, the symbol $\boldsymbol{t}$ denotes the unit tangent vector, which is the derivative of the position vector with respect to arc length. The tangent vector is shown in (Figure 4), and always points in the direction of increasing arc length. By definition, it is perpendicular to the instantaneous radius of curvature, ρ. This radius of curvature always points in the direction

of the principal normal, or $\boldsymbol{n}$ in (Figure 4) [6, 8, 9]. The principal normal points towards the center of curvature and is of unit length.

Together, the principal normal and the tangent vector define the osculating plane [6, 9]. This is the plane in which the osculating circle is found. The osculating circle is a virtual circle which shares the same center and instantaneous radius of curvature as a point on *C*. The orientation of the osculating plane therefore changes with the orientation of the osculating circle. Imagine *C* in the figure curving towards the negative $\boldsymbol{x}_3$ direction, as shown, and then turning back upwards towards the positive $\boldsymbol{x}_3$ direction. This would cause the direction of $\boldsymbol{n}$, which lies in the osculating plane and points towards the center of the osculating circle, to flip about *C* when the direction of the curve changes. This relationship is imperative to understanding one-dimensional curvature, because the curvature vector always points in the direction of the principal normal.

Recall that the tangent vector is the derivative of the position vector with respect to arc length. Taking the second derivative with respect to arc length yields the curvature vector, or $\boldsymbol{\kappa}$. The curvature is shown in (Figure 4), and its mathematical definitions are shown below.

$$\boldsymbol{\kappa} = \frac{d\boldsymbol{t}}{ds} = \frac{d^2\boldsymbol{x}}{ds^2} \tag{5}$$

$$\kappa\,\boldsymbol{n} = \frac{dt}{ds}\,\boldsymbol{n} \tag{6}$$

$$\kappa = \frac{1}{\rho} \tag{7}$$

As stated, the curvature vector is the derivative of the tangent vector with respect to arc length, and the second derivative of the position vector with respect to arc length. The scalar quantity of curvature is simply κ and is the inverse of the instantaneous radius of curvature. The scalar κ can be thought of as a measure of the degree to which *C* is curving. Essentially, it is the rate of change of the tangent vector as it travels along *C* in the direction of increasing u. The curvature vector will always point in the same direction as the curve itself, or the same direction as the principal normal.

This relationship between curvature vector and the curve itself is critical to the utility of a curvature measurement for the purposes of shape sensing. If both the curvature direction and magnitude are known at a point on an inflatable, then the profile of the local area about that point can be estimated. This is the strategy employed by NASA's FBG chain, which will be discussed at length in the coming section. By taking curvature measurements at many points on the inflatable surface, the entire profile can be interpolated and thus defined, to a certain degree of accuracy. Of course, the accuracy of this method could be improved by placing more sensors in the same space and thereby reduce the amount of error present due to interpolation. Additionally, more sensors could be placed at specific points of interest across the body, such as a point of a mounting interface. This would be similar to the practice of increasing the density of finite elements around points of high stress concentration or complex geometry when performing finite element analysis. When employed properly, the curvature readings from the surface of an inflatable can become a powerful means of sensing its shape.

At this point, it is important to reiterate that the curvature quantity discussed above is a vector, which points in a single direction by definition. This is due to the nature of the curve itself; it only possesses a single dimension, length, and thus can only experience curvature in one direction at a time. Regardless of the direction or degree to which *C* is curving, at each individual point along *C*, the curvature is only ever a vector which acts along a single direction. This means that any method which utilizes simple curvature measurements would only capture a single profile or cross section of the total surface. An inflatable body's surface is after all two-dimensional, and additional sensors would need to be placed in multiple directions to detect the curvature in more than one dimension. This will prove to be the motivation for the second part of this investigation, which will be discussed in subsequent sections.

2.2. Contemporary Methods for Sensing Curvature

2.2.1. Fiber Bragg Gratings and the NASA Effort

One of the most accurate means of sensing curvature with intrinsic embedded sensors, available today, involves the use of fiber optic strain gages, also known as Fiber Bragg Gratings. These are sections in a fiber optic cable which have been specially treated to exhibit different refractive properties than the rest of the cable. A length of fiber, which is made of glass, has a certain refractive index associated with its optical density. The variation of refractive index with radial position is the reason why fiber optic cables are able to transmit data; the interior index is so high that complete internal reflection occurs along the length of the fiber. So, if a light source enters one end of the fiber, it will reach the far end of the fiber with minimal loss of intensity. Some loss may occur around tight

bends in the cable, as these essentially reduce the angle required for the light to be transmitted out of the surface of the fiber.

Typically, it is desirable for the refractive indices of the various layers of a fiber to be uniform along the length. Any deviation would be viewed as a defect in the fiber. However, in an FBG, the refractive index of the core is intentionally altered to create regions of higher optical density. There are several methods for fabricating FBGs, but all of them make use of UV light to alter the refractive index of the fiber [10]. During the manufacturing process, the center of a fiber is doped with a photosensitive compound. These doping compounds typically include Germanium and cause the center of the fiber to be sensitive to permanent change via UV radiation [10, 11]. Holographic or interferometric methods will split UV laser light into two separate beams, and then recombine them to produce an interference pattern on the fiber [10]. This pattern, often comprising thousands of fringes, reacts with the doping compound within the fiber. Any region of the fiber exposed to the UV light has its refractive index permanently altered [10, 11]. The spacing of these regions can be adjusted by changing the interference pattern. Other, noninterferometric, methods make use of periodic pulses of UV light, or shine UV light through a specially designed phase mask to activate the doping compound within the fiber and produce the desired regions of high optical density. A grating is a collection of many such regions; when the spacing of these regions is chosen to correspond with a specific wavelength, it is known as a Fiber Bragg Grating [10, 11]. When a spectrum of light is shown on one end of the fiber containing an FBG, this predetermined wavelength, known

as the Bragg wavelength, will be reflected back to the source end. The following figure gives a depiction of this process (Figure 5).

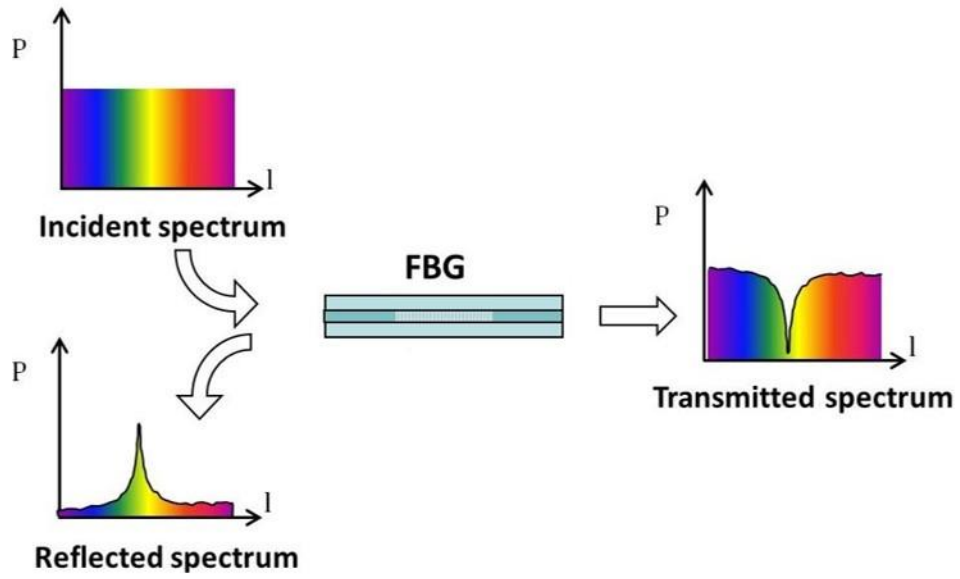

Figure 5: FBG Operating Principle [12]

Note that the reflected peak is returned to the end of the fiber into which the incident spectrum is shown. This means that only one end of the fiber need be connected to an interrogating device, a particularly useful characteristic for remote sensing of structures or inflatables. The peak in the above graphic shows the Bragg wavelength (λ_B), which is related to the fringe spacing (Λ) within the grating by the following equation:

$$\lambda_B = 2n\Lambda \tag{8}$$

In this equation, n signifies the effective index of refraction of the grating. This refractive index is subject to change with the conditions affecting the fiber [13].

Specifically, if the FBG experiences a mechanical strain or a change in temperature, the effective index of refraction will change. This change can be quantified, and thus the strain or temperature variance can be measured. The following equation gives the relationship between wavelength shift ($\Delta\lambda/\lambda_o$) and strain (ε) and temperature change (ΔT).

$$\frac{\Delta\lambda}{\lambda_o} = k\,\varepsilon + \alpha_\delta\,\Delta T \tag{9}$$

The k term is known as the gauge factor, and is generally approximately 0.78. The gauge factor is a constant which allows one to determine the strain associated with a change in wavelength. The term α_δ is the change in refractive index with respect to temperature. Although the temperature sensing capabilities of FBGs are impressive, they are not included in this study. This essentially means that the term on the far right of the above equation can be neglected. That term applies to the change in refractive index, and thus wavelength, caused by the temperature change. Provided there is no temperature change during the straining process, then there is no effect on the wavelength. It should be noted that the strain term above is actually a combination of mechanically caused strain and strain due to temperature change [14]. Not only does the index change due to mechanical strain, but as the temperature of the FBG changes, it undergoes thermal expansion or contraction. This accounts for an additional strain contribution, which can complicate attempts to measure purely mechanical strain. Fortunately, just as the thermal effects on the refractive index, as long as the temperature change is insignificant, then so are its effects on the

wavelength shift. Without the impact of temperature, the only factor influencing wavelength shift is the mechanical strain, which is illustrated in the figure below (Figure 6).

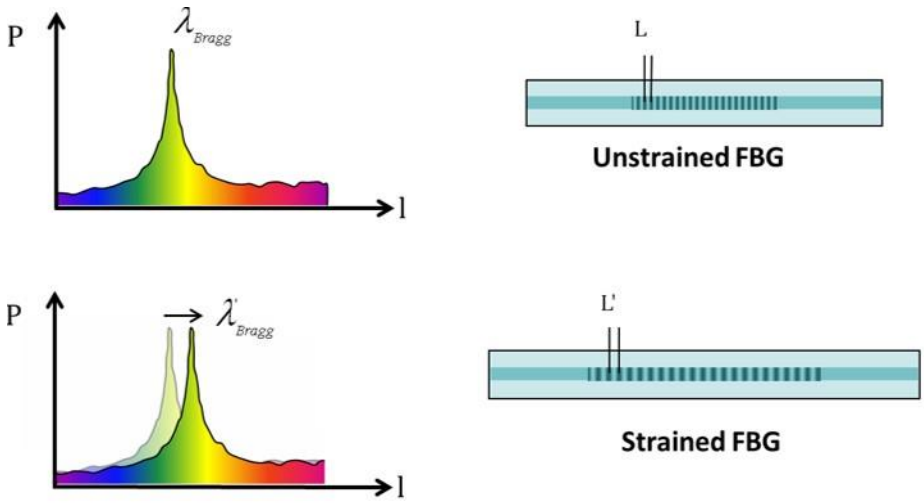

Figure 6: Effect of Strain on Wavelength [15]

This figure demonstrates the reflected peak, which is the Bragg wavelength, shifting to a longer wavelength as the FBG is stretched. The reverse is also true; as the FBG is compressed, the peak will shift towards a shorter wavelength, resulting in a negative value for the calculated shift. By measuring this shift, one can determine the amount of strain present in the fiber.

Obtaining a measure of the curvature from FBGs is directly related to measuring the strain. In fact, a curvature reading simply requires two FBGs on either side of the curve and a known separation distance. Imagine a beam that is bending with one FBG on the outside of the bend, and another on the inside. The outer FBG will be in tension, while the inner FBG will be in compression. This will result in a positive strain for the FBG in

tension, and a negative strain for the FBG in compression. If the thickness of the beam is known, then the curvature is the difference in the two strains divided by the beam thickness [5]. This is a simple relationship derived from the geometry of the Bernoulli-Euler Beam model, where plane sections perpendicular to the centroidal axis remain planar and perpendicular to the centroidal axis after deformation. This relationship is written in the following equation.

$$\frac{\Delta\varepsilon}{d} = \frac{\varepsilon_2 - \varepsilon_1}{d} = \frac{1}{\rho} = \kappa \tag{10}$$

The d term is the distance or thickness separating the FBGs. The assignment of ε_1 and ε_2 can be arbitrary in this case, as the hypothetical beam was given no orientation. For a surface, the strain measured in the FBG on the top of the surface would typically be assigned to ε_2. This ensures that a convex curve of the surface exhibits positive curvature, while a concave portion of the surface would exhibit negative curvature. Note that by taking the difference between the two strains, any common stretching behavior in the direction of the FBGs is eliminated. The equation above is the governing principle of the FBG chain used by NASA in their shape sensing research.

The NASA project is truly a revolutionary method of shape sensing. Although similar to the beam bending problem discussed above, this technique is far more complex. Instead of using just two FBGs, the NASA project makes use of three separate cores, all of which contain strain-sensing FBGs [5]. By using three strain measurements at any given

point along the cable, this device can detect any direction of curve experienced by the cable. Recall the beam example, which used only two FBGs. As long as the beam was bending such that the FBGs were on either side of the curve, then those two would suffice. However, if the beam were to bend in a new direction orthogonal to its original bend direction, the two FBGs would no longer be on either side of the curve. Any curvature associated with this in-plane bending of the beam would be impossible to detect with the current configuration. This is why the NASA cable has three separate cores; regardless of the bend direction, the curving behavior of the cable can always be captured. With the curvature measured, one can essentially work backwards to determine the shape of the cable. NASA uses similar equations to the ones introduced in the section of this paper discussing space curves, known as the Frenet-Serret formulas, to perform these calculations [5, 6]. This is how the NASA FBG chain can be used to generate a virtual image of the cable itself. Thus, the FBG chain is capable of measuring a curve in any single direction, and the only limitation on its accuracy in this respect is the number of FBGs along the cable.

In order to place a large number of FBGs within the length of their cable, NASA turned to a technique known as multiplexing. This is typically done to increase the number of signals that can be sent through a fiber. A device called a multiplexer separates an incident spectrum of light into specific wavelengths that are then shone into one end of the fiber. On the far end of that same fiber, another device interrogates the now many wavelengths of light and their associated data. This greatly increases the amount of information that can be sent through a single fiber, which is why NASA chose to employ

this technique. Multiplexing with FBGs does not require an initial multiplexer, because each FBG can be written to reflect a different wavelength. By writing many FBGs, each with a unique wavelength, into a single fiber, the requirement of multiplexing is fulfilled [13]. The resulting fiber can be thought of as a chain of FBGs. Not only does each FBG measure strain independently of the others in the chain, but each unique wavelength corresponds to the position along the curve at which that FBG can be found. The three multiplexed FBG chains thus allow researchers at NASA to know both the location and curvature of many points along the cable. This is why the computer generated image in (Figure 3) looks nearly identical to the chain itself. It is a very powerful technique for measuring curvature due to the high accuracy of the FBGs.

Despite the numerous advantages afforded by the NASA fiber optic cable, this method is still limited in its shape sensing capabilities. Because the cable is in essence a space curve, it can only ever experience curvature in one direction at a time. This means it can only measure a single direction of curvature at a time. As previously stated, the geometry of a surface cannot be captured by a single component of curvature. In order to provide more than just a profile of the inflatable surface, the NASA FBG chain must weave back and forth across an area multiple times. When the virtual image of the chain used in this manner is generated, one can glean a general understanding of the surface geometry. However, surface details are lost between the bends of the cable. Additionally, any inaccuracies of the method, such as those caused by twist within the fiber, distort the image created by the computer. Although recent developments suggest that NASA can now account for twist within the cable, the underlying shortcomings of their shape sensing

method persist. This is due to the nature of the method itself. The fiber cable can sense its own curvature very accurately, but this is not equivalent to the curvature of the surface upon which it rests. While the cable method can provide a qualitative depiction of a surface, it cannot be used to quantify the curvature of that surface. This requires a distinct approach to the problem of shape sensing; one which measures the curvature of the surface and not simply a space curve. With an accurate measure of the surface geometry at multiple points about an inflatable, the geometry of the spaces between sensors could be inferred. With the current NASA method, the regions in between cable runs are completely unmeasured, and researchers can only guess as to their precise geometries.

A more comprehensive approach to shape sensing requires the measuring of three components of curvature on the surface. This requires the fabrication of a novel sensor array specifically designed to measure the curvature of a surface. With enough of these new sensors placed about an object, the complete geometry can be known, and the inflation process can be monitored. As a proof-of-concept exercise, an inflation controller was designed to receive inputs in the form of curvature measurements and use them to control the flow of air into an inflatable. In this preliminary study, the selected curvature sensors were of the conductive ink type. These bend or flex sensors, as they are also known, are discussed in the next section.

2.2.2. Conductive Ink Based Flex Sensors

Although the accuracy of FBGs makes them highly valued for shape sensing, an economic alternative is the flex sensor. 2 This flexible potentiometer provides a variable electrical resistance which depends on the amount of bend present in the body of the sensor.

The sensor body, or substrate, is made from a material which is both flexible and electrically insulating [16]. A conductive ink is then applied to the substrate. Once dried, this conductive ink becomes a connection between two electrical contacts. The figure below shows a typical conductive ink type flex sensor with a loop of wire attached to its contacts (Figure 7).

Figure 7: Flex Sensor Made With Conductive Ink [17]

As the substrate is bent, the conductive ink is strained longitudinally and experiences a reduction in its cross sectional area. Moreover, the conductive ink begins to crack and from gaps as it is deformed [16]. Both of these behaviors contribute to an increase in the electrical resistance of the potentiometer. This change in resistance is proportional to the amount of deflection of the substrate. The following figure shows three potential configurations of a bend sensor and the associated changes in resistance (Figure 8).

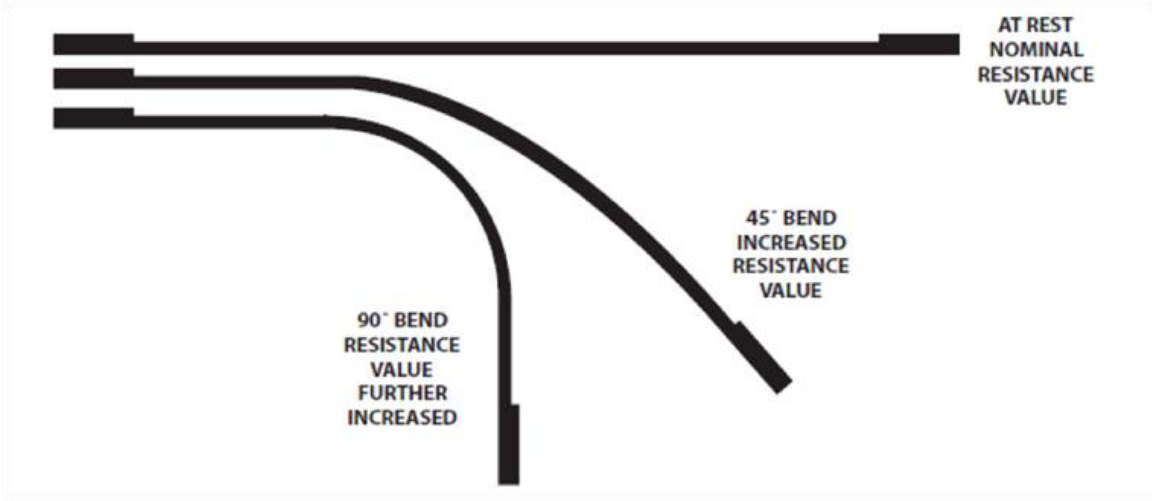

Figure 8: Flex Sensor Behavior [18]

The process depicted above occurs in a predictable manner, and the resistance fluctuation can be measured simply by applying a voltage across the two contacts.

In order to measure curvature using a flex sensor, one must calibrate each sensor individually. This is because the exact process by which the conductive ink cracks and deforms is unique to each sensor. A simple method of calibration employs test surfaces of known curvature. With a known voltage applied, the flex sensor is shaped to fit the curved surface, and the resulting voltage change is recorded. By performing this process for a number of known curvature values, the flex sensor can be calibrated. A number of test surfaces are required. While the resistance varies in a repeatable manner, it does not vary linearly with the bending of the substrate. This necessity for individual calibration is one of several disadvantages encountered with the use of flex sensors.

Another prominent shortcoming of the flex sensor is the nature of its variable resistance. As the sensor is bent, the resistance change is a result of an average amount of

curvature present in the substrate. Depending on the surface which it measures, the substrate could be severely bent on the end closest to the contacts and relatively flat on the end furthest from the contacts. This would yield a specific increase in resistance, which could then be measured. However, the exact same resistance change could be caused by the reverse situation, with a flat portion near the contacts and a severe curve on the far end. There is also a configuration in which the substrate experiences a consistent amount of curvature which would yield the same exact resistance change. Thus, a simple voltage drop caused by a flex sensor is not enough to define the curvature of a surface; it will only give an average reading of the curvature in the substrate. Fortunately, this issue can be largely overcome by choosing an appropriate size for the flex sensor. Due to its design, the flexile potentiometer can be produced in a multitude of sizes. This allows one to select a flex sensor which is relatively small when compared to the surface it will be measuring. In this case, an average reading of curvature will likely be representative of the curve present on the surface in the area immediately surrounding the flex sensor.

Another disadvantage comes from the fact that the flex sensor is once again a one-dimensional curve. Just as the NASA cable, a flex sensor can only provide a reading of curvature in a single direction. So once more, a new method of curvature must be developed which captures the curvature of a surface, not just a space curve.

Despite these disadvantages, there are several reasons to justify the use of flex sensors in shape sensing applications. For one, the flex sensor itself is relatively robust. When compared to an FBG, the flex sensor substrate can withstand a far greater amount of physical trauma that may occur during the inflation process. In addition, the average flex

sensor is far less expensive to manufacture when compared to an FBG. They are also considerably easier to use in a controller application; flex sensors can be reduced to simple analog voltage inputs whereas FBGs require sophisticated interrogation equipment and software. For these reasons, the flex sensors were chosen for a prospective inflation controller, which is the focus of the next section.

2.3. Curvature-Based Inflation Controller

2.3.1. Design Objectives and Theory

The current need for accurate shape sensing of inflatables is based on the notion that an inflatable can be monitored and its inflation controlled. As a preliminary investigation into this quandary of improving shape sensing, a Curvature-Based Inflation Controller was designed. The goal of this CBIC was to serve as a proof of concept for the potential application of a novel shape sensor. Successful operation of the inflation controller would then justify additional study in the field of shape sensing.

The main objective of the controller was to autonomously inflate an initially deflated body to desired final inflation level. This final inflation level would be measured solely by sensing the shape of the inflatable, as opposed to using a pressure gauge or some other technique. This distinction is important for two reasons; (1) for a successful design, it would support the notion of using shape sensing, and (2) it makes this controller unique.

In order to use contemporary shape sensing methods as the only source of feedback, several assumptions were necessary. First, it was assumed that the body in question contained regions that could be described by the simple, one-dimensional, curvature. This

is because the current shape sensing techniques only allow for the measurement of one direction of curvature at a time. This assumption is easily justified, as there are many possible inflatable geometries which contain one or more regions characterized by a single direction of curvature. Such regions are referred to as parabolic points, and will be discussed further in the next chapter. However, a simple example of a parabolic region is the side body of a cylinder. The only direction of curvature is in the plane of the circumference of the cylinder. So, for this simple geometry, a single dimension of curvature could suffice to sense its shape, assuming the body inflates uniformly, and no unexpected bending or folding occurs. This is the essence of the second main assumption for the controller design: that the inflation process itself is spatially smooth, and no unexpected complications arise during inflation. Essentially, the inflation process must occur such that the measured regions are initially flat, and gradually become more curved as the body is inflated. The maximum curvature of these regions will be reached only when the body is fully inflated, and not before. This also assumes that no portion of the body will inflate more quickly than the rest, as this would again lead to curvature in more than one direction at a time, which cannot be captured at present. With these assumptions defined, the controller could be designed.

The first step in designing this inflation controller was the selection of the inflatable object itself. A child-sized air mattress was chosen for its relatively simple geometry, ease of inflation control, and low cost. For instance, the sides of the air mattress exemplify the desired parabolic geometry. In addition, the internal structure of the mattress is somewhat representative of that of inflatable space structures, with multiple chambers designed to

hold its shape. Finally, the material of the mattress is useful as it limits the amount of stretching within the surface itself. While it is not fabric-reinforced as many inflatable space structures are, the vinyl of the air mattress does not stretch in an appreciable amount during the process of routine inflation. This is important, as the type of deformation of interest is curvature, and excessive stretching could potentially skew sensor readings.

With the inflatable chosen, the selection of the remaining parts was relatively straightforward. The choice of actuator, or air pump in this case, was obvious. The air mattress was accompanied by a small air pump which could be plugged into a 120VAC power supply. This pump would be operated by a relay, which would interrupt the power going to the pump when the mattress was fully inflated.

The relay would then be controlled by a programmable Arduino board, which was chosen for its ease of operation. The figure below shows the control loop used for the design of the CBIC (Figure 9).

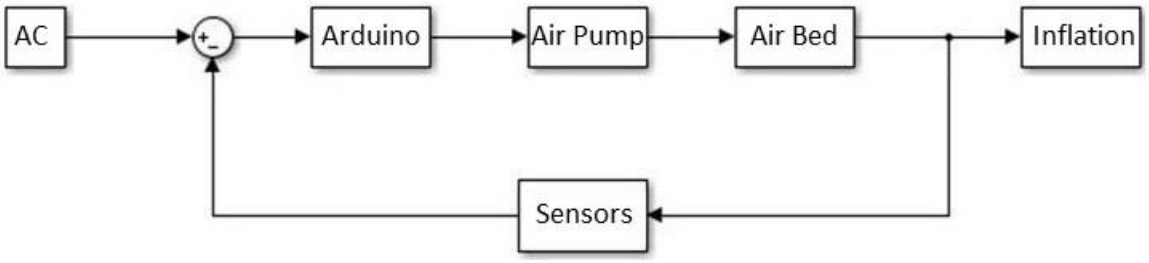

Figure 9: CBIC Control Loop

As shown on the left of the figure above, the control loops begins with the AC power supply, in this case a wall outlet. The Arduino controller then operates the relay, which allows the actuator, an air pump, to be powered. The plant is of course the air mattress,

which is inflated by the air pump. As the mattress inflates, the flex sensors detect the curvature at specified points. The Arduino board then uses this sensor feedback to turn the relay off once the desired level of inflation is achieved. Although not particularly powerful, this Arduino board could be easily programmed to carry out the task of operating the relay based on the shape sensor input. In a sense, the relatively minimal computing power of the Arduino was ideal for demonstrating the overall simplicity of the CBIC. This simplicity is surely a desirable attribute in space applications, where so many complex systems exist and quantities like voltage and CPU usage are strictly rationed.

As previously stated, the shape sensing technique employed by the CBIC was the flexible potentiometer, or bend sensor. These were chosen for both their durability and availability. Given that the precise conditions of the inflation process are still largely unknown, the plastic resin substrate of the flex sensors made them the conservative choice. In addition, the flex sensor technology has existed for decades, making them widely available and relatively low in cost. These factors made flex sensors the logical choice for sensing curvature with the CBIC.

Once the control loop was designed, and the parts chosen, the complete CBIC system could be designed. The final design is shown in the figure below (Figure 10).

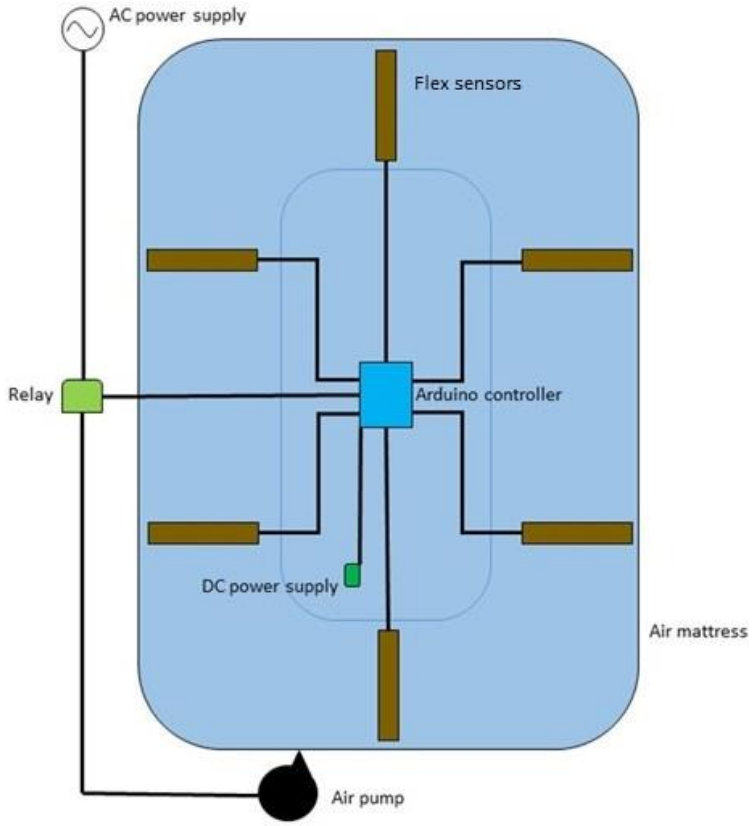

Figure 10: CBIC Final Design

Note the positions of the flex sensors, chosen to ensure that regions of simple curvature would be measured. Additionally, the central position of the Arduino board was chosen for the convenience of routing the wires from each sensor to the board. The small DC power supply for the Arduino depicted above is in fact a 9V battery. The combined weight of the components in the center of the mattress was deemed to be inconsequential to the inflation process. The procedure for constructing and testing the above design is documented in the next section.

2.3.2. Fabrication and Testing

The first part of the CBIC to be completed was the circuit required to collect curvature measurements with the flex sensors. A simple voltage divider would allow one to measure a potential difference across the flex sensor, and thus the curvature reading. The next step involved connecting the circuit to the Arduino board, which naturally needed to be programmed to read and display the data from the flex sensor. Once a functioning code was written, the analog voltage from the flex sensor could be viewed in the serial monitor, a feature built in to the Arduino programming software. This allowed the flex sensor to be calibrated using precisely cut wooden blocks of known curvature.

The code was then extended to include six separate sensors. The complete Arduino code can be found in the Appendix. The routine is essentially a while-loop which maintains voltage to a relay as long as at least one of the six sensors is reading a value below a predetermined threshold. The purpose of the while loop was to ensure that any minor asymmetry of the inflation process would be accounted for. If one or more portions of the mattress reached their defined maximum before the rest, the controller would continue to inflate until all regions had reached their threshold values. These threshold values would correspond to a level of curvature that was consistent with the desired level of inflation. The same code was used to set the threshold values; the code contains instructions for the displaying of sensor data in the serial monitor. Because every flex sensor differs slightly in terms of overall resistance, each of the six sensors used in the CBIC required its own threshold value. With the flex sensors attached to the air mattress, the controller was turned on and the relay allowed power to be supplied to the air pump. Initially, provisional

threshold values were deliberately set high so that they were never reached. This allowed the air mattress to become fully inflated while the analog voltage signals from all six sensors were displayed in the serial window. When the desired level of inflation was reached, the displayed analog voltage values were recorded and used to set the threshold values for the subsequent experiments.

Testing of the CBIC was initiated by simply connecting the DC power supply to the Arduino board. The two states of the air mattress, before and after the inflation process, are shown in the figure below (Figure 11).

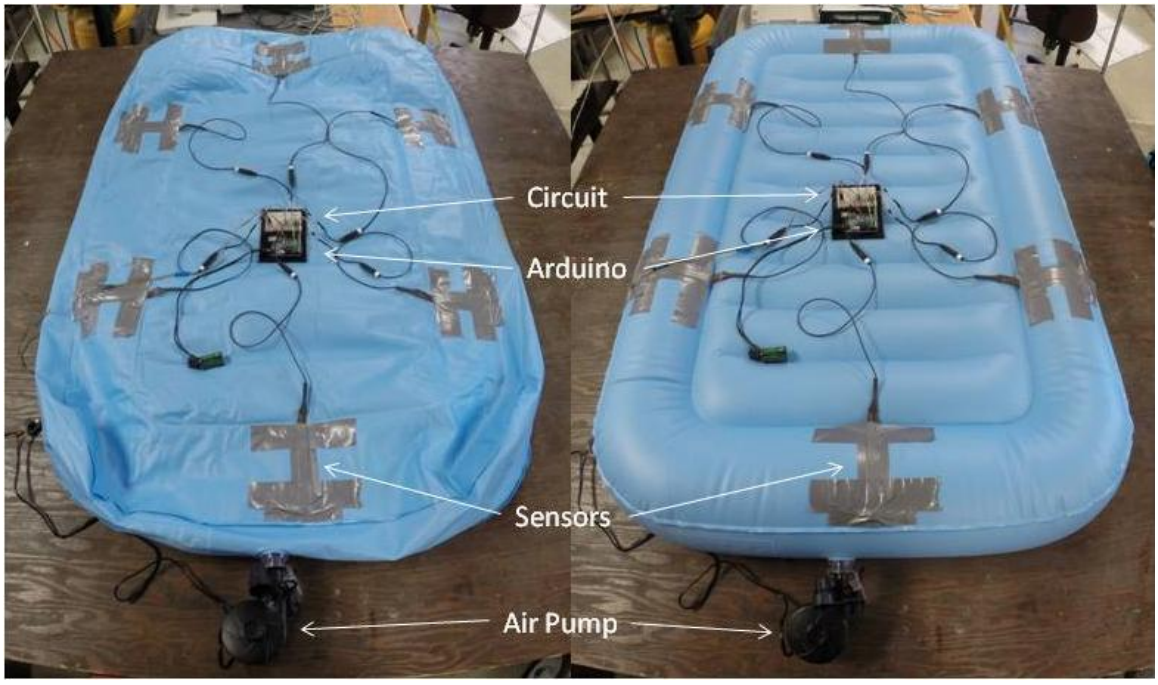

Figure 11: CBIC Inflation Test - Before and After

The image on the left hand side shows the initial, deflated state, while the image on the right hand side shows the final, inflated state. Once powered, the Arduino controller operated the relay, and the air pump began to inflate the air mattress. During the inflation

process, the flex sensors detected increasing curvature values in the specified regions around the inflatable body. The Arduino continually monitored the status of the flex sensors to ensure that continued inflation was necessary. After several minutes, the flex sensors began to detect curvature that was consistent with the desired level of inflation. When all six sensors had reached their defined threshold values, the controller switched the relay off. This shut down the air pump, and the inflation process was terminated.

2.3.3. Results and Discussion

The outcome of the CBIC test described above was on the whole positive; the controller performed as expected, and the overall goal was achieved. The mattress was fully inflated as desired, and the only feedback received by the controller was that of shape sensing. In a binary assessment of whether or not it was successful, the CBIC test was indeed successful. This result has implications, as well as several important caveats.

The major implication of the test result is this: the strategy of controlling inflation by means of shape sensing is apparently a viable one, with many potential applications space inflatables. For its relatively simple design, the CBIC was effective at inflating the air mattress to the desired inflation level. Due to its design, the CBIC could even be adapted to inflate other bodies with differing geometries. The code could easily be altered to vary the number of sensors being used to sense the inflatables' shapes. There would have to be regions of simple curvature, just as the air mattress, but this is not an unlikely assumption. Provided the body could be first inflated to set the sensor threshold values, the CBIC could control any subsequent inflation. Of course, many different inflation

controllers could be designed to be more robust than the CBIC. However, these results certainly aid in justifying any endeavor to develop more sophisticated controllers.

Despite the overall success of the CBIC test, there are numerous aspects of the CBIC which require improvement. As mentioned above, the CBIC design is very simple. This is an advantage from certain perspectives, but can be a disadvantage in the context of shape determination. While the method for shape sensing employed by the CBIC was sufficient for this laboratory test, it is likely that the system would not function properly in the field. Recall the original motivations for using shape sensing over other means of inflation control feedback, such as pressure gauges: whereas current methods assume a spatially smooth inflation process without any unexpected behavior, shape sensing would not. The true advantage to shape sensing should be the capacity to diagnose any potential issue before it becomes problematic. Unfortunately, the CBIC requires the same type of gradual, well-behaved inflation process as most modern methods in order to be successful. Any unforeseen complications in the inflation process could potentially cause the CBIC to fail. Moreover, once inflated, there are many problems that could arise which would go undetected by the CBIC. This is a combined result of both the method of shape determination and the limited utility of the shape sensors themselves.

The CBIC's shape sensing technique relied heavily on the simplicity of both the inflatable's geometry and the inflation process. Due to the low number of sensors employed, there were large regions of the air mattress whose behavior was uncaptured. For instance, it is possible that folding could occur between the flex sensors and go unnoticed by the controller. Because it uses curvature measurements to determine inflation

progress, the CBIC is technically employing a shape sensing method. However, the CBIC falls short of actually determining the overall geometry of the inflatable. At no point in the inflation process did the controller identify or make use of the actual values of the curvatures being measured by its sensors. Such information was not necessary for this simple test, as both the inflation process and the final geometry were well understood. This would certainly not be true of the inflation of an actual space structure in the field, and thus a more sophisticated means of shape determination is required. The true goal of shape sensing is to identify the geometry of a body at any stage, without relying on its final geometry or a smooth inflation process. This requires not only quantifying the curvature of the body at many points, but an intelligent control system which can use these curvature readings to assemble a virtual depiction of the body. Recall the NASA FBG chain and its computer-generated image. This is the functionality required of shape sensing systems in order to detect any unforeseen complications during inflation, as well as continue to monitor the overall health of the inflatable.

The overall shape determination strategy was not the only shortcoming of the CBIC. The flex sensors that were used are far from ideal in terms of accurately measuring curvature. As stated in a prior section, the flex sensors are prone to errors along their length due to an averaging effect. This prevents them from being able to distinguish a region of constant curvature from a region of multiple curvatures whose average is being detected. Again, this is a result of the flex sensors being mere potentiometers and not specifically calculating a true value for the curvature, as FBG shape sensing methods do.

It is important to note that while FBG techniques for sensing curvature do in fact calculate a value based on the sensor data, they are not an all-encompassing solution for the limitations of the CBIC. This is because both FBG pairs and flex sensors are incapable of sensing curvature in more than one direction at a time. This means that the geometry of a body will be largely undetermined, as the curvature in the directions orthogonal to the sensors could not be measured. Capturing this information for a surface would require a novel shape sensor, with the capacity to measure curvature in multiple directions.

If such a sensor could be developed, there would be many advantages over the current methods. One could gain a detailed understanding of a two-dimensional surface without any prior knowledge about the geometry. This would require no preliminary phase to set threshold values for curvature, because this new sensor would actively detect and monitor curvature. By employing these novel sensors about an inflatable, the true geometry of the body could be known in real time. The proposed capabilities are beyond that of modern flex sensors, as well as contemporary FBG curvature-sensing techniques. This new sensor would be instrumental in monitoring both the inflation and overall health status of an inflatable. The second portion of this project is an investigation into the development of such a sensor.

CHAPTER 3: CURVATURE IN MULTIPLE DIRECTIONS

3.1. The Geometry of a Surface

The primary objective of the new curvature sensor is to capture the geometry of the surface of an inflatable as opposed to merely that of a space curve. In order to fully explore this distinction, the mathematical definition of a surface will now be introduced. Additionally, the concept of curvature as it pertains to a surface will be discussed.

A surface is a two-dimensional entity which exists in three dimensions. It can be thought of as a thin sheet of paper, whose thickness is insignificant compared to its other two dimensions. The sheet extends in two directions, yet it can bend and curve through space. For any surface *S* in three-dimensional space, the location of any point can be described by its Cartesian coordinates. These coordinates are expressed as a position vector $\boldsymbol{x}$, just as for a space curve. However, instead of $\boldsymbol{x}$ being a function of a single parameter u, the position vector of a surface depends on two distinct parameters, u_1 and u_2. These are curvilinear coordinates which can vary with time and are assigned to the surface itself. The following expression gives the position of a point on *S* as a function of curvilinear coordinates [8, 9].

$$\boldsymbol{x} = \boldsymbol{x}(u_1, u_2) = x_1(u_1, u_2)\boldsymbol{e}_1 + x_1(u_1, u_2)\boldsymbol{e}_2 + x_3(u_1, u_2)\boldsymbol{e}_3 \qquad (11)$$

Once again, the $\boldsymbol{e}_i$ terms denote the unit vectors in the three Cartesian directions. The u_i terms span the surface in different directions; if they were to describe the same direction, then u_1 is equal to u_2 and the surface simplifies to a space curve. When either u_1 or u_2 is

constant along a curve on *S*, it is known as a parametric curve or coordinate curve [8, 9]. Together, the parametric curves of u_1 and u_2 form a virtual net on *S*, just as lines of latitude and longitude cover the surface of the Earth [9].

A surface can be defined as the set of points described by a function f of the three Cartesian coordinates, as shown below [8].

$$f(x_1, x_2, x_3) = 0 \tag{12}$$

Many surfaces can be written such that a single coordinate x_i is a function of the other two coordinates. This form is shown in the following equation [8].

$$x_3 = f(x_1, x_2) \tag{13}$$

This form requires that for each ordered pair (x_1, x_2), there is exactly one value of x_3. This would be indicative of a surface which rises and falls yet never doubles over or covers itself. A specific example of this form is the hyperbolic paraboloid, given by the following equation:

$$x_3 = \frac{{x_1}^2}{a^2} - \frac{{x_2}^2}{b^2} \tag{14}$$

The terms a and b are constants. The following figure shows a hyperbolic paraboloid, or saddle surface (Figure 12).

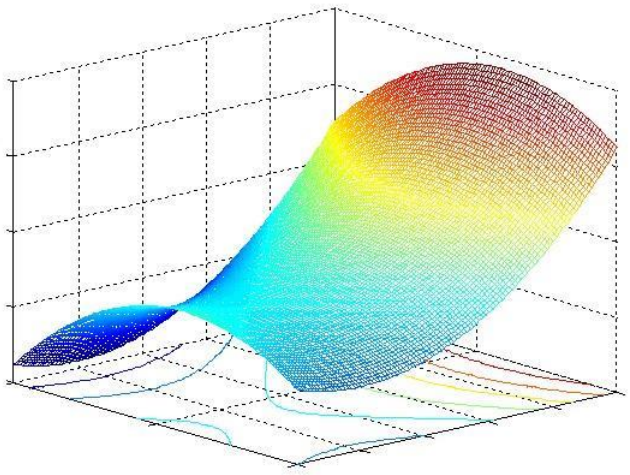

Figure 12: Hyperbolic Paraboloid

The saddle surface in the figure above is important to this discussion of curvature, as it exhibits positive curvature in one direction and negative curvature in the other.

In order to discuss the curvature of a surface, we will proceed formally, following the explanation of Kreyszig [8]. When describing a surface, it is useful to establish a metric. A metric of a surface is a tool which allows us to take measurements of that surface. The particular metric of interest is the element of arc, ds. This is a basic unit for measuring arc length, and is unique to the geometry which it describes. Beginning with the one-dimensional case of a space curve, the Pythagorean Theorem leads to the following expression for the element of arc:

$$ds^2 = dx_1{}^2 + dx_2{}^2 + dx_3{}^2 \tag{15}$$

$$ds^2 = d\boldsymbol{x} \cdot d\boldsymbol{x} \tag{16}$$

Since $\boldsymbol{x} = \boldsymbol{x}(u_1, u_2)$, the above derivative must be taken with respect to both surface parameters, as shown below.

$$d\boldsymbol{x} = \frac{\partial \boldsymbol{x}}{\partial u_1} du_1 + \frac{\partial \boldsymbol{x}}{\partial u_2} du_2 \tag{17}$$

This leads to the following expression for the element of arc ds [7]:

$$ds^2 = \left(\frac{d\boldsymbol{x}}{du_1} du_1 + \frac{d\boldsymbol{x}}{du_2} du_2\right) \cdot \left(\frac{d\boldsymbol{x}}{du_1} du_1 + \frac{d\boldsymbol{x}}{du_2} du_2\right) \tag{18}$$

This can be rearranged in the form of a quadratic in du_1 and du_2:

$$ds^2 = \frac{d\boldsymbol{x}}{du_1} \cdot \frac{d\boldsymbol{x}}{du_1} (du_1)^2 + 2 \frac{d\boldsymbol{x}}{du_1} \cdot \frac{d\boldsymbol{x}}{du_2} du_1 du_2 + \frac{d\boldsymbol{x}}{du_2} \cdot \frac{d\boldsymbol{x}}{du_2} (du_2)^2 \equiv \mathrm{I} \tag{19}$$

The above expression is known as the first fundamental form of a surface. This is an invariant, meaning that for the given surface, ds will be constant value regardless of coordinate convention. The coefficients in the above expression are the components of the first fundamental tensor, or metric tensor g_{ij}, shown below [8, 9, 19, 20].

$$\mathcal{g}_{ij} = \begin{bmatrix} \mathcal{g}_{11} & \mathcal{g}_{12} \\ \mathcal{g}_{21} & \mathcal{g}_{22} \end{bmatrix} = \begin{bmatrix} \frac{d\boldsymbol{x}}{du_1} \cdot \frac{d\boldsymbol{x}}{du_1} & \frac{d\boldsymbol{x}}{du_1} \cdot \frac{d\boldsymbol{x}}{du_2} \\ \frac{d\boldsymbol{x}}{du_2} \cdot \frac{d\boldsymbol{x}}{du_1} & \frac{d\boldsymbol{x}}{du_2} \cdot \frac{d\boldsymbol{x}}{du_2} \end{bmatrix} = \begin{bmatrix} E & F \\ F & G \end{bmatrix} \tag{20}$$

Here, the symbols E, F, and G are typically used for convenience. Because the scalar product of two vectors is commutative, the terms $\mathcal{g}_{12}$ and $\mathcal{g}_{21}$ will always be equal. The metric tensor can be used to describe a surface by its first fundamental form.

The curvature of a surface depends not only on the first fundamental form, but the second fundamental form as well. The second fundamental form is given by the following expression [8].

$$-d\boldsymbol{x} \cdot d\boldsymbol{N} \equiv \text{II} \tag{21}$$

$$-\frac{d\boldsymbol{x}}{du_1} \cdot \frac{d\boldsymbol{N}}{du_1}(du_1)^2 - 2\frac{d\boldsymbol{x}}{du_1} \cdot \frac{d\boldsymbol{N}}{du_2} du_1 du_2 - \frac{d\boldsymbol{x}}{du_2} \cdot \frac{d\boldsymbol{N}}{du_2}(du_2)^2 \equiv \text{II} \tag{22}$$

Here, $\boldsymbol{N}$ refers to the surface normal, which differs from the principal normal of Section 2.1. The surface normal is perpendicular to the tangent plane at a point on the surface and is found by taking the cross product of the two derivatives of $\boldsymbol{x}$ with respect to the surface parameters u_1 and u_2 [8, 19]. It can be found via the following equation.

$$\boldsymbol{N} = \frac{\frac{d\boldsymbol{x}}{du_1} \times \frac{d\boldsymbol{x}}{du_2}}{\left|\frac{d\boldsymbol{x}}{du_1} \times \frac{d\boldsymbol{x}}{du_2}\right|} \tag{23}$$

The second fundamental form is also an invariant. Its coefficients are the components of the tensor of the second fundamental form, b_{ij}, shown below [8, 9, 19, 20].

$$b_{ij} = \begin{bmatrix} b_{11} & b_{12} \\ b_{21} & b_{22} \end{bmatrix} = \begin{bmatrix} -\frac{d\boldsymbol{x}}{du_1} \cdot \frac{d\boldsymbol{N}}{du_1} & -\frac{d\boldsymbol{x}}{du_1} \cdot \frac{d\boldsymbol{N}}{du_2} \\ -\frac{d\boldsymbol{x}}{du_2} \cdot \frac{d\boldsymbol{N}}{du_1} & -\frac{d\boldsymbol{x}}{du_2} \cdot \frac{d\boldsymbol{N}}{du_2} \end{bmatrix} = \begin{bmatrix} e & f \\ f & g \end{bmatrix} \tag{24}$$

Just as for the first fundamental tensor, b_{ij} is assigned the symbols e, f, and g for convenience. Also, as shown above, b_{ij} is symmetric, meaning that b_{12} is equal to b_{21}.

Both fundamental forms I and II are characteristics of the surface itself, and their ratio is the scalar normal curvature, κ_n [8]. This is shown in the equation below [8, 9, 19, 20].

$$\kappa_n = \frac{\text{II}}{\text{I}} = \frac{-d\boldsymbol{x} \cdot d\boldsymbol{N}}{d\boldsymbol{x} \cdot d\boldsymbol{x}} = \frac{e(du_1)^2 + 2f du_1 du_2 + g(du_2)^2}{E(du_1)^2 + 2F du_1 du_2 + G(du_2)^2} \tag{25}$$

This is the mathematical definition of the normal curvature of a surface, which is the same as the one-dimensional curvature of the space curve from Section 2.1. In the case of the surface, κ_n is specific to the direction of the tangent vector, which defines the direction of

the curve, and incorporates the second derivative of position with respect to movement along the surface. For any point on *S*, there are an infinite number of curve directions and associated curvatures. To find the normal curvature for any given tangent vector, the Weingarten Equations must be used [19]. These equations use the two fundamental forms to construct a third tensor κ_{ij} which describes the complete state of curvature for a point on a surface. This tensor is often called the Shape Operator, but can also be referred to as the Weingarten Map or the tensor of curvature. The Weingarten Equations, and the associated Weingarten tensor are given below [19, 20].

$$\kappa_{11} = \frac{fF - eG}{EG - F^2} \tag{26}$$

$$\kappa_{12} = \frac{gF - fG}{EG - F^2} \tag{27}$$

$$\kappa_{21} = \frac{eF - fE}{EG - F^2} \tag{28}$$

$$\kappa_{22} = \frac{fF - gE}{EG - F^2} \tag{29}$$

$$\kappa_{ij} = \begin{bmatrix} \kappa_{11} & \kappa_{12} \\ \kappa_{21} & \kappa_{22} \end{bmatrix} \tag{30}$$

In the case of orthogonal surface coordinates u_1 and u_2, the above tensor is symmetric so that $\kappa_{12} = \kappa_{21}$ [19]. It is the κ_{ij} entities which are readily measurable by a localized sensor array, which is the motivation for this particular investigation.

This tensor of curvature can define the curvature of a surface at a point based on a chosen tangent vector. The maximum and minimum curvatures are given by the

eigenvalues of κ_{ij}, and are called the principal curvatures. These are denoted as κ_1 and κ_2, and their corresponding eigenvectors $\boldsymbol{v}_1$ and $\boldsymbol{v}_2$ are known as the principal curvature directions [8, 9, 19, 20]. These principal curvatures define the geometry of the surface for which they are found. For this reason, they are extremely important to the goal of shape sensing. By measuring the curvature in three different directions simultaneously, one can construct the shape operator for a surface and thus find the principal curvatures. Additionally, the tensor of curvature can potentially be used to find the fundamental forms of a surface and establish a metric by which to measure said surface.

Other definitions for the curvature of a surface exist, but these typically incorporate the principal curvatures. For instance, the Gaussian curvature K is defined as follows [8]:

$$K = \kappa_1 \kappa_2 = \frac{b}{\mathscr{g}} \tag{31}$$

The terms b and $\mathscr{g}$ are the determinants of the tensors b_{ij} and $\mathscr{g}_{ij}$, respectively. The Gaussian curvature is useful for classifying the type of surface geometry present, as its sign changes depending on the signs of κ_1 and κ_2. Another commonly used expression is the mean curvature H, which is defined below.

$$H = \frac{1}{2}(\kappa_1 + \kappa_2) \tag{32}$$

The mean curvature is simply the arithmetic mean of the two principal curvatures. It quite literally gives an average value for the curvature of a surface at a point. Like the Gaussian curvature, the mean curvature can be positive, negative, or zero, depending on the surface. This is because different surface geometries have differing principal curvatures.

κ_1 and κ_2 can be positive or negative, and their associated directions are almost always perpendicular to each other. The following figure shows several surfaces and their principal curvature directions (Figure 13).

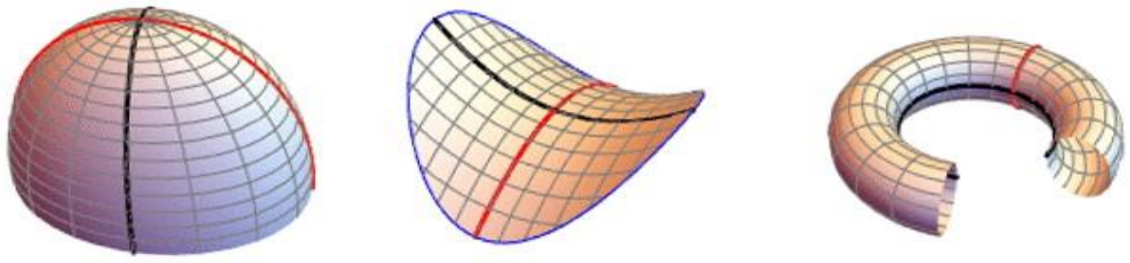

Figure 13: Principal Curvature Examples [21]

In each of the above cases, the point for which the principal curvatures are shown is the intersection of the red and black lines. The black line follows the direction of the minimum curvature, and the red line depicts the maximum curvature. For the object on the far left, both principal curvature values are positive. The remaining two surfaces each have a minimum curvature which is negative, assuming the convention in which the surface normal extends outward from the surface and not into the surface. The signs of the principal curvatures can be used to classify various surface geometries.

There are three possibilities regarding the signs of the principal curvatures of a surface. The first is the case where both κ_1 and κ_2 have the same sign, such as on the first body in (Figure 13). This point is called an elliptic point, and it can be identified as having a dome-like geometry. Spheres exhibit a special case of elliptic geometry; because all directions have equal curvature, all directions are principal curvature directions. Additionally, all points on a sphere are umbilics, which are points on a surface for which all directions contain principal curvatures. This is the only time that the directions associated with κ_1 and κ_2 are not necessarily perpendicular, as every direction is a principal curvature direction. For any elliptic point, the Gaussian curvature K is always positive. This is true for both convex and concave surfaces, as the principal curvatures will always have the same sign, regardless of convention.

The next type of surface geometry is called a parabolic point. These are points at which one of the principal curvatures is equal to zero. Technically, there is an additional geometry classification for which both κ_1 and κ_2 are zero. This is trivially a plane, for which the expected curvature would always be zero. As discussed in Section 2.3.1, a simple example of a parabolic surface is the side of a cylinder, which experiences no curvature in the longitudinal direction. Parabolic points are characterized by a nonexistent Gaussian curvature; when either κ_1 or κ_2 is zero, then so is the product of these two principal curvatures.

The final classification of surface geometry is a hyperbolic point, which is characterized by two nonzero principal curvatures of opposite sign. The saddle geometry in (Figure 12) and the remaining two surfaces in (Figure 13) portray this type of geometry.

The Gaussian curvature of a hyperbolic point will always be negative due to the sign difference in κ_1 and κ_2. Saddle curves are of particular interest to this study, as the two opposing curvatures are not easily captured by contemporary sensing methods. Using either FBGs or flex sensors in their contemporary configurations, only one principal curvature could be measured, leaving much of the surface unknown. This is of course assuming that the sensors are intentionally aligned with the principal curvature directions. If the sensors were placed such that the curvature in a non-principal direction was measured, the resulting measurement would be less useful for determining the surface geometry. This is true for any of the three geometry classifications listed here, but especially for the hyperbolic point.

In order to determine the shape of a surface, the curvature must be measured in more than one direction. It is particularly useful to measure the curvature in known directions of principal curvature. If the principal curvature values are known, then the shape of the surface can be determined. By starting with the principal curvatures and essentially working backwards, the underlying geometry of the surface could be inferred. This is not unlike the method employed by the NASA FBG chain effort discussed in Section 2.2.1. However, successful shape determination of a two-dimensional surface requires curvature measurements to be taken in multiple directions simultaneously. This in turn requires a novel sensor array, which was developed as the second major task in this investigation. The design, fabrication, and testing of this new surface curvature sensor are discussed at length in the next section.

3.2. Sensing Curvature in Multiple Directions

3.2.1. Design Objectives and Theory

The purpose of the proposed sensor array is to capture the curvature of a surface. The objective of this design was then to measure curvature in multiple directions at one time. Specifically, this array was designed with two sensors that could take curvature readings in two separate, orthogonal directions. These would be aligned with the principal curvature directions of a test surface in order to ascertain the geometry thereof. Additionally, the curvature in the direction between the two principal directions would be measured by a third sensor. This would help to bridge the gap between the two principal curvatures and shed additional light on the geometry of the surface. This sensor configuration is consistent with that of a strain-sensing rosette, the measurements from which can be used to construct the strain tensor. The rosette layout was chosen for this application in order to take the measurements necessary to construct the metric tensor for a surface. From this, along with the principal curvatures, the fundamental forms could be derived and the shape of the surface defined. Because the rosette configuration was implemented in its design, this novel sensor array will be referred to as the Curvature-Sensing Rosette (CSR).

Once the basic concept of the CSR was formulated, the specific method of curvature detection was chosen. In light of the limitations of the CBIC due to the inaccuracy of its flex sensors, the FBG method was selected for use in the CSR. As stated previously, this method requires two FBGs separated by a known distance in order to measure curvature. The CSR was designed to be a patch of known thickness with three

FBGs attached to either side of it. This patch could either be affixed to the surface of an inflatable, or the sensor configuration could be embedded in the inflatable material itself. The six FBGs form three separate pairs, each capable of sensing curvature in a single direction. The CSR would then be able to measure curvature with a high level of accuracy in three different directions simultaneously. The FBG pairs would also eliminate additional strain due to stretching, as this behavior on one side would get cancelled out by the other.

In order to test the accuracy of the CSR, a test surface of known geometry is used. A surface with hyperbolic geometry was chosen for testing, as it could best demonstrate the utility of the CSR. In order to be defined, the opposite principal curvatures of the saddle surface would require a sensor which could detect curvature in multiple directions. Provided the shape of the saddle surface could be detected, the CSR could be tested on various other geometries.

Ideally, the CSR could be applied to any surface without prior knowledge of the geometry. Recall that the surface, metric, and Weingarten tensor are all defined with respect to a pair of orthogonal coordinates, u_1 and u_2. If the directions of u_1 and u_2 are aligned with the principal curvature directions, then the tensor of curvature simplifies to a diagonal matrix comprised of the principal curvatures, as shown below.

$$\kappa_{ij} = \begin{bmatrix} \kappa_{11} & \kappa_{12} \\ \kappa_{21} & \kappa_{22} \end{bmatrix} = \begin{bmatrix} \kappa_1 & 0 \\ 0 & \kappa_2 \end{bmatrix} \tag{33}$$

As it stands, the two orthogonal sensor pairs are intended to align with the principal curvatures. However, assuming enough information can be gathered by the CSR about the

surface geometry, then the direction of the principal curvatures need not be known. The Weingarten tensor of curvature could be constructed by performing a coordinate transformation on the measurements taken by the CSR.

Consider a single pair of orthogonal coordinates u_1 and u_2, with directions $\boldsymbol{e}_1$ and $\boldsymbol{e}_2$, respectively. Rotated an angle θ about the origin is a new set of orthogonal coordinates, u_1' and u_2', with directions $\boldsymbol{e}_1'$ and $\boldsymbol{e}_2'$, respectively. This is illustrated in the figure below (Figure 14).

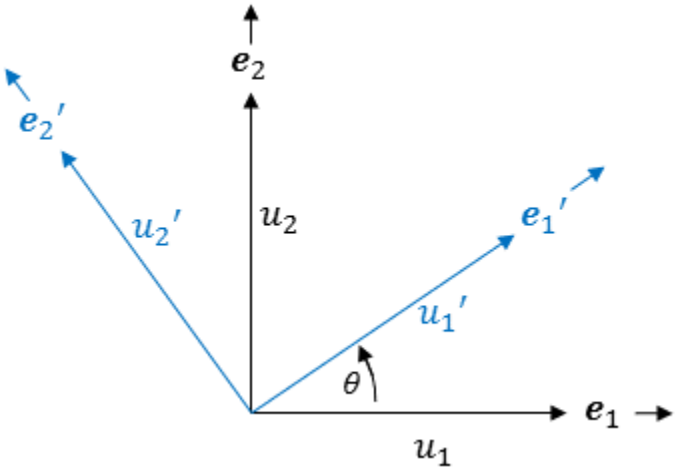

Figure 14: Rotation of Coordinate Axes

In some cases, it may be convenient to establish a new set of coordinates which simplify calculations. In order to transform the original coordinates into the new prime coordinates, the direction cosine matrix is used. This matrix gives a mapping from the original coordinates to the new set, and is based on the angle between the two coordinate systems. This transformation matrix is shown below.

$$a_{ij} = \begin{bmatrix} \boldsymbol{e}_1{}' \cdot \boldsymbol{e}_1 & \boldsymbol{e}_1{}' \cdot \boldsymbol{e}_2 \\ \boldsymbol{e}_2{}' \cdot \boldsymbol{e}_1 & \boldsymbol{e}_2{}' \cdot \boldsymbol{e}_2 \end{bmatrix} = \begin{bmatrix} cos\theta & sin\theta \\ -sin\theta & cos\theta \end{bmatrix} \tag{34}$$

Recall that the curvature tensor is formulated using the two fundamental forms, which are invariants. This means that the curvature tensor is also an invariant and thus does not change even as the coordinate system does. So, the curvature tensor κ_{ij} can be transformed into $\kappa_{ij}{}'$ using the following equation, without affecting the tensor itself.

$$[\kappa_{ij}{}'] = [a_{ij}]^T [\kappa_{ij}] [a_{ij}] \tag{35}$$

In the above equation, the superscript '*T*' denotes a transposed matrix. With this equation, the curvature measurements from the CSR can be transformed into another coordinate system, such as the principal coordinates. These are the set of axes which are aligned with the principal directions.

In order to obtain κ_{ij} from three arbitrary curvature measurements, one must utilize an inherent property of the Weingarten Map, which gives a value of normal curvature for any specified tangent direction [19, 20]. Suppose a curvature sensing rosette was placed on a surface with parameters u_1 and u_2. The following figure illustrates this (Figure 15).

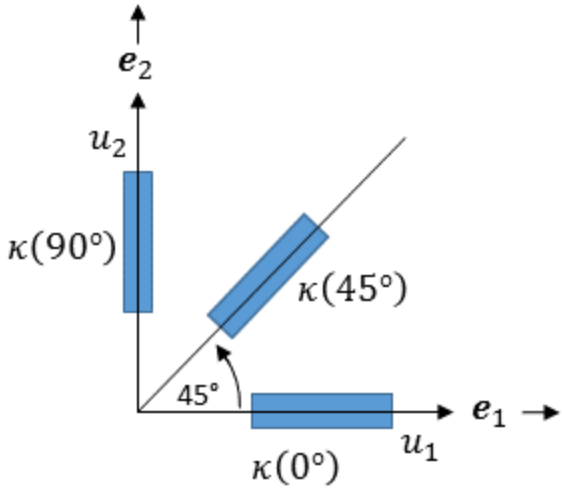

Figure 15: CSR on Coordinate Axes

Note that the three blue rectangles show where the curvature sensing FBG pairs would be. These FBG pairs give curvature readings of $\kappa(0°)$, $\kappa(45°)$, and $\kappa(90°)$ as shown. By choosing an arbitrary coordinate system aligned with the direction of $\kappa(0°)$, we can write the following [19, 20].

$$\kappa(0°) = \boldsymbol{e}_1 \cdot \kappa_{ij} \cdot \boldsymbol{e}_1 \tag{36}$$

$$\kappa(0°) = \begin{bmatrix} 1 & 0 \end{bmatrix} \begin{bmatrix} \kappa_{11} & \kappa_{12} \\ \kappa_{21} & \kappa_{22} \end{bmatrix} \begin{bmatrix} 1 \\ 0 \end{bmatrix} = \kappa_{11} \tag{37}$$

Note that equations (36) and (37) are equivalent, because $\begin{bmatrix} 1 \\ 0 \end{bmatrix}$ is the coordinate representation of the unit vector $\boldsymbol{e}_1$. By aligning the surface coordinate axes with the first FBG pair, the first term in the curvature tensor is instantly found. Similarly, the κ_{22} term can be found with the following expressions.

$$\kappa(90°) = \boldsymbol{e}_2 \cdot \kappa_{ij} \cdot \boldsymbol{e}_2 \tag{38}$$

$$\kappa(90°) = [0 \quad 1] \begin{bmatrix} \kappa_{11} & \kappa_{12} \\ \kappa_{21} & \kappa_{22} \end{bmatrix} \begin{bmatrix} 0 \\ 1 \end{bmatrix} = \kappa_{22} \tag{39}$$

Again, this is the utility of the Weingarten curvature tensor. In order to find the final component, the vector in the direction of the central FBG pair must be used.

$$\kappa(45°) = \left(\frac{\sqrt{2}}{2}\boldsymbol{e}_1 + \frac{\sqrt{2}}{2}\boldsymbol{e}_2\right) \cdot \kappa_{ij} \cdot \left(\frac{\sqrt{2}}{2}\boldsymbol{e}_1 + \frac{\sqrt{2}}{2}\boldsymbol{e}_2\right) \tag{40}$$

$$\kappa(45°) = \frac{1}{2}[1 \quad 1] \begin{bmatrix} \kappa_{11} & \kappa_{12} \\ \kappa_{21} & \kappa_{22} \end{bmatrix} \begin{bmatrix} 1 \\ 1 \end{bmatrix} \tag{41}$$

$$\kappa(45°) = \frac{1}{2}[\kappa_{11} + 2\kappa_{12} + \kappa_{22}] \tag{42}$$

Equation (42) can be written as such because the curvature tensor is symmetric for all orthogonal coordinate systems, so $\kappa_{12} = \kappa_{21}$. Now the known values for κ_{11} and κ_{22} can be substituted into equation (42), and the final component of the curvature tensor can be found.

With the Weingarten curvature tensor known, the principal curvatures and their directions can be found. With these directions known, the local area surrounding the CSR could be defined. By placing multiple CSRs about an inflatable, the overall shape can be determined. This is the intended long-term use for the CSR. The scope of this project, however, only included testing of the CSR on a controlled test surface.

3.2.2. Fabrication and Testing

This section details the process by which the proposed CSR was produced and subsequently tested. As a preliminary experiment, a single FBG pair was constructed and its accuracy tested. A sample specimen was affixed with an FBG (FBGS SG-01) on either side. This specimen was clamped to a wooden test block of known curvature. The FBGs were connected to an Optical Sensor Interrogator (OSI) (National Instruments PXIe-4844), which performed the action of sending a spectrum of white light down the two fibers and recording their respective reflected peaks. With data acquisition software capturing the FBG behavior, the test specimen was bent from an initially straight position to match the curve of the wooden block. This experimental setup can be seen in the figure below (Figure 16).

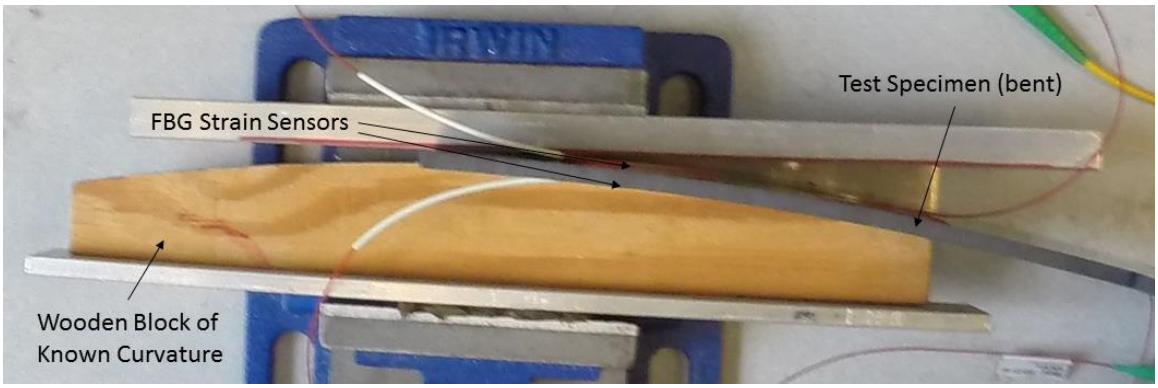

Figure 16: FBG Bend Test Setup

The process of bending the specimen to the wooden block, then back to true was repeated several times. The data collected from the test are shown in the following graph (Figure 17).

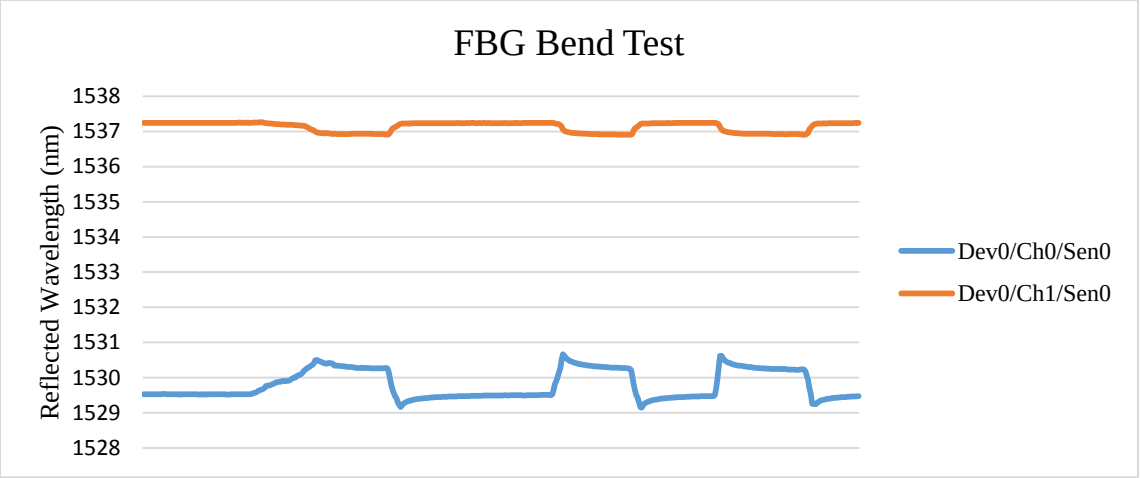

Figure 17: Bend Test Data

In the graph above, the vertical axis shows the wavelength of the reflected peaks of each of the FBGs throughout the test. The horizontal axis is arbitrary time; as none of the primary results are time-dependent, the units were omitted. Note that the order of the two data series on the graph is merely a result of the wavelengths of the reflected peaks of each FBG. The legend shows which data series corresponds to each sensor channel. In this case, the orange data were collected from the FBG in compression, or the FBG on the bottom of the test specimen in (Figure 16). This means that the blue data corresponds to the FBG on the top in (Figure 16), which would be in tension during the bending portion of the test. This is easily seen in the behavior of the data sets. A peak in the lower line on the graph corresponds to a fully bent specimen, which would result in the maximum tension being applied to the FBG on the top in (Figure 16). This occurs during a trough in the upper line on the graph, which corresponds to the maximum compression of the FBG on the bottom in (Figure 16). As previously stated, the test specimen was bent, then

straightened, then bent again. From the graph, it can be seen that this procedure was performed a total of three times before the test was concluded. The values of the wavelengths of the reflected peaks before and after one such bending procedure, as well as the calculated strain, are tabulated below (Table 1).

Table 1: FBG Bend Test Data

Sensor Channel	λ_o (nm)	λ (nm)	ε
0	1529.526	1530.668	0.000934
1	1537.245	1537.053	-0.000157

The values for λ_o were chosen from the first flat portion of the graph, before the specimen was subjected to bending. The λ values were taken from a time corresponding to a peak in the lower data series. This represents the time when the maximum bending, and thus curvature, occurred. Using the FBG equation (9) found in Section 2.2.1 and ignoring the effects of temperature, the strain ε in each FBG was calculated from the measured wavelength shift. Note that these particular FBGs had a gauge factor of 0.799, as opposed to the standard value of 0.78. This was provided by the manufacturer and had no impact on the outcome of the test. By taking the difference in strain $\Delta\varepsilon$ between the top and bottom FBGs, and then dividing through by the thickness of the test specimen, an experimental value for the curvature was obtained. The results of this initial test are shown in the following table (Table 2).

Table 2: FBG Bend Test Results

$\Delta\varepsilon$	κ_{exp} (mm^{-1})	κ_{act} (mm^{-1})	Accuracy (%)
0.0010904	0.002647	0.002625	99.17

The value for the true or actual curvature κ_{act} was found by taking the inverse of the known radius of the wooden block, which was 381 mm (15 inches), the inverse of which is 0.002625 mm^{-1}. As shown in the table, the accuracy of this method was found to be 99.17%, meaning that the experimental value for curvature was within one percent of the actual value. This level of accuracy is expected of FBGs. In fact, minor inaccuracies of the wooden test block could just as easily be responsible for the less than one percent discrepancy as the FBGs. In any case, the accuracy of the FBG method of sensing curvature was deemed acceptable for the CSR.

In order to successfully fabricate the CSR as designed, the above process would need to be repeated three-fold. This would require a total of six FBGs, which exceeds the number of available ports on the OSI by two. A multiplexed FBG chain was used to circumvent this issue. This custom-ordered multiplexed fiber was comprised of sixteen FBGs, each of which had a unique wavelength for its reflected peak. These wavelengths varied from 1,510 to 1,590 nm, as this was the operating range of the OSI. The wavelength values of the FBGs progressed in order with increasing distance along the length of the fiber. Thus, the location of each FBG in the multiplexed chain could be determined by its wavelength.

The rosette design was measured out and drawn on the surface of the intended material for the CSR. A vinyl patch from a swimming pool repair kit was chosen for its flexibility and resilience to tearing. The multiplexed fiber was looped around the rosette design so that all six necessary FBGs could be aligned with their respective axes. The alignment of the FBGs in the CSR can be seen in the following figure (Figure 18).

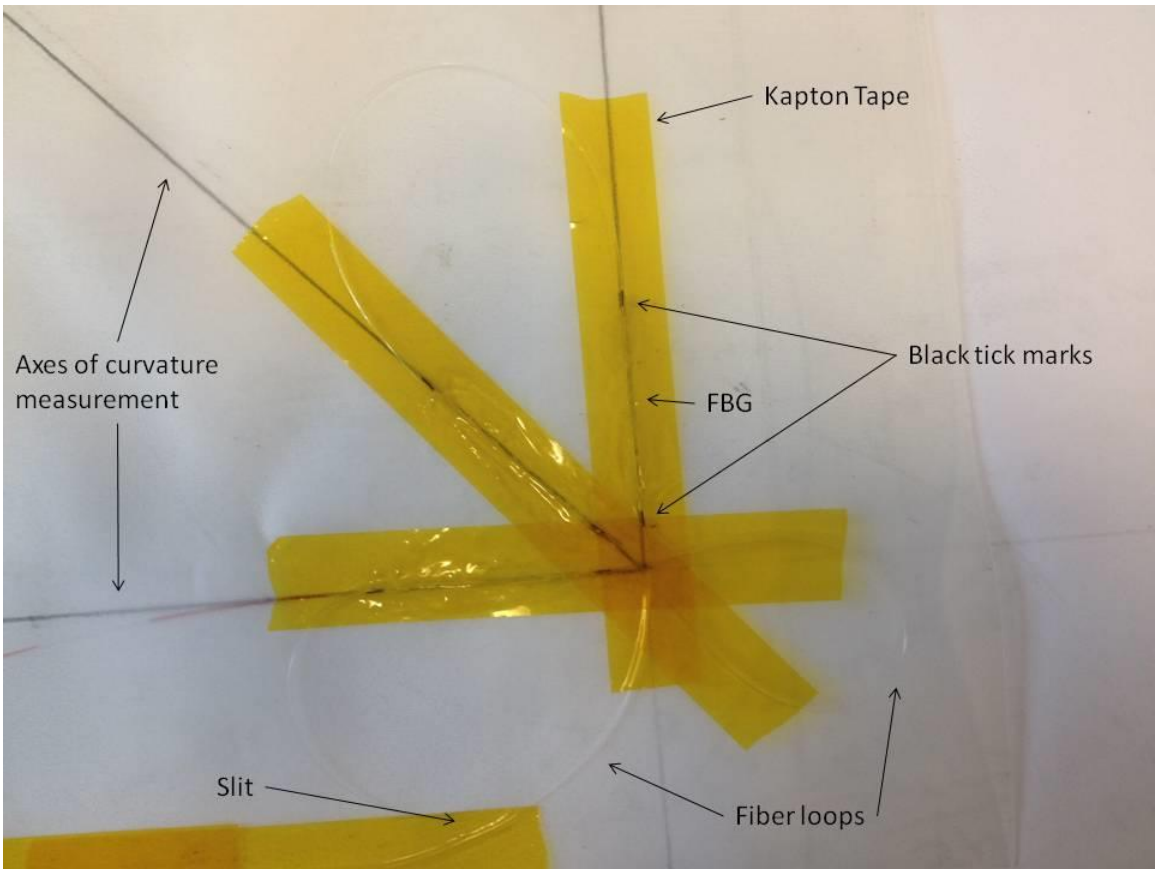

Figure 18: Curvature Sensing Rosette

The three straight lines in the image above are the three directions along which the curvature will be measured. The clear fiber can be seen looping about these lines, ensuring that each FBG is positioned correctly. A thin slit was cut in the vinyl to allow the fiber to pass from one side of the patch to the other, so that three of the FBGs could be attached to the back side. The location of each FBG in the fiber is labeled with two black tick marks separated by approximately 1.5 inches; the FBG is located in between these marks. By securing the tick marks to the specified axes, the FBGs were guaranteed to lie on said axes. Several adhesives were tested for this application, based on recommendations made in [22].

In the end, cyanoacrylate adhesive was used to secure the fiber to either side of the vinyl patch along the drawn lines. Pressure sensitive tape (Kapton) was used to secure the fiber beyond the glued portion in order to protect the fragile loops from potential damage. The fabrication of the prototype CSR was thus completed and ready for testing.

While the construction of the CSR was relatively straightforward, the subsequent testing proved to be far more problematic. Finding a suitable saddle surface with which to calibrate the CSR was much more difficult than anticipated. It is true that saddles exist as a part of several common geometries, such as a torus. However, actually finding a saddle whose geometry could be quantified for testing purposes was a challenge. It was originally proposed that a section of an inflatable torus be outfitted with the sensor throughout a full inflation procedure. This would only serve as a qualitative test, as the only way to quantify the curvature of the saddle during inflation would be to employ the exact type of sensor being tested.

Moreover, initial testing showed that the CSR would not be usable on many available surfaces. This is due to the nature of the multiplexed FBG chain and the OSI to which it is connected. When the FBG chain is connected to this OSI, the sixteen reflected peaks are easily detected by the software. In the configuration window, one can set specific ranges in which a peak of interest, such as the six peaks that comprise the CSR, might be found. An example of this window is shown in the figure below (Figure 19).

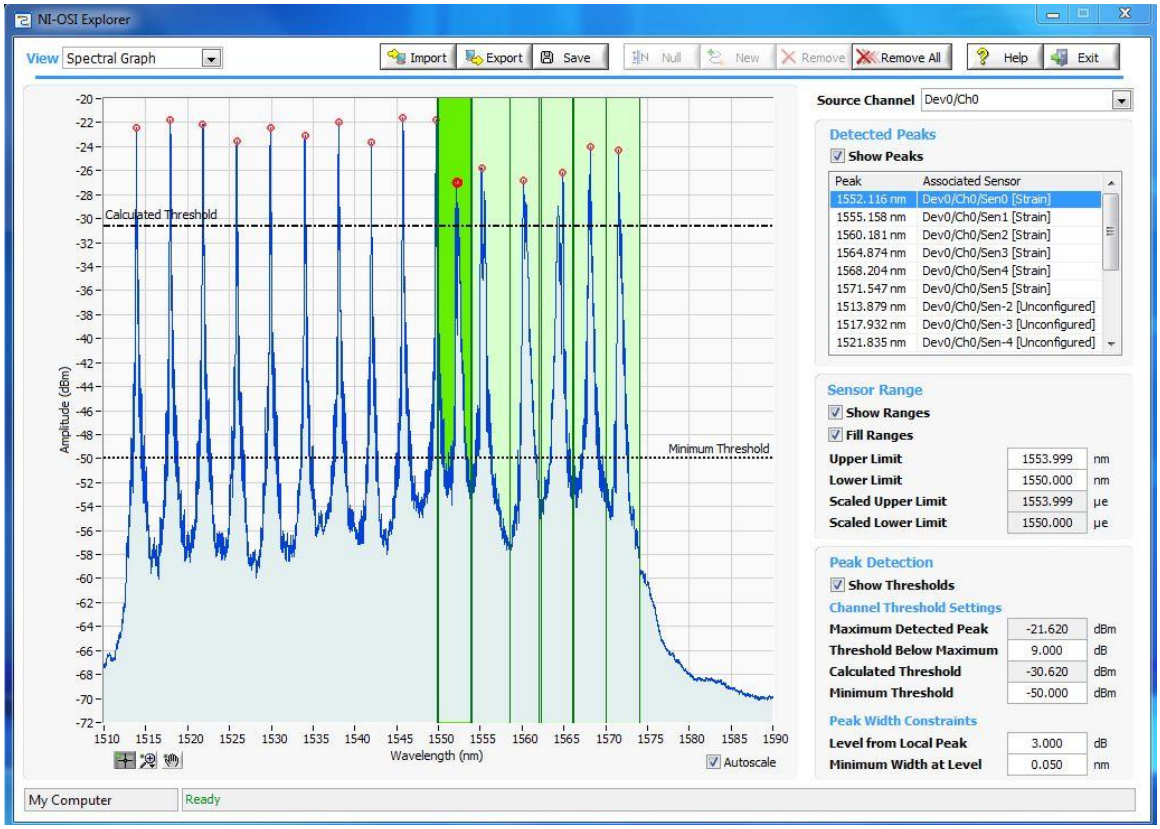

Figure 19: OSI Configuration Mode

The green regions are those which are defined by the user to contain peaks of interest. Any peak not within a predefined range shows up as an unconfigured sensor. In order for the data acquisition software to record the behavior of a peak, it must be a configured sensor. This is of no major consequence in theory; each peak can exist in its own range due to the multiplexing of the fiber. However, the method of strain sensing using FBGs requires that the peaks undergo a wavelength shift, which can be used to determine the strain present in the fiber at that point. FBGs can be extremely accurate due to the sensitivity of the sensor. In this case, the FBGs were so sensitive to any strain caused by curving that one or more of the peaks associated with the CSR would shift out of the range for which it was

configured. This immediately causes the peak(s) in question to become unconfigured, meaning they cannot be measured by the software. There are a few means of solving this problem, but most of these require an entirely new multiplexed FBG chain to be used in place of the current one. This was not a viable option for a number of reasons. There was, however, a solution which could also solve the problem of finding a suitable test surface.

The proposed solution involved the designing of a test surface using CAD software, which could then be 3-D printed for experimentation. In this way, an ideal saddle surface could not only be produced, but the exact principal curvatures would be defined in the CAD software. More importantly, the curvature of the test surface could be deliberately set to a very low value. This would ensure that the wavelength shift would be minimal, yet still measureable for FBGs. The issue regarding the unconfigured sensor peaks was only a problem for most surfaces because the amount of curvature present on those surfaces was enough to cause the peaks to shift out of their predefined ranges. However, by defining low principal curvature values, the measured peaks would be able to shift a detectable amount without shifting beyond their allowed range. Additionally, from a theoretical standpoint, detecting a very shallow curve would demonstrate the accuracy of the CSR much better than would a severe curve.

Using the CAD program Solidworks, the test saddle surface was designed. This geometry was achieved by revolving the two-dimensional profile of a circle about another circle which lay in a plane perpendicular to the first. This produced a virtual torus, the inner surface of which exhibits saddle geometry. The majority of the torus was then 'cut' away, leaving a small section with saddle geometry. The radii of the original two circles

were defined as 50 inches (1,270 mm) and 60 inches (1,524 mm), which would also be the radii of curvature of the saddle surface. The principal curvatures would then be the reciprocals of these radii, or -1/50 in^{-1} (-1/1,270 mm^{-1}) and 1/60 in^{-1} (1/1,524 mm^{-1}), respectively; the definition of the saddle surface dictates that the principal curvatures must be of opposite sign. This ensured that the curvatures detected by the CSR would be both minimal and distinct, to further demonstrate its capabilities. In order to ensure that the CSR patch would conform to the test saddle surface exactly, a male and female pair of saddles were designed. The idea is to place the CSR between the two compatible saddles, then press them together and force the CSR to mimic their shape. The virtual male saddle and the pair of saddles are shown in the figure below (Figure 20).

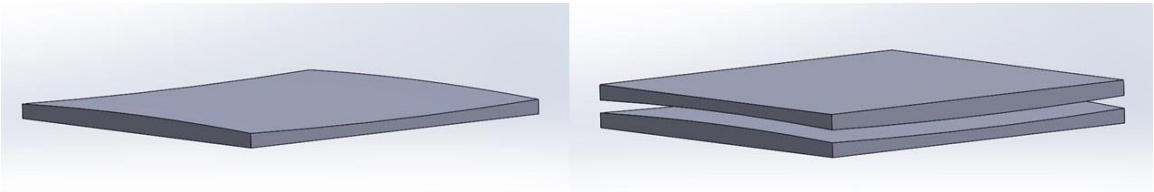

Figure 20: Virtual Saddle Surfaces in Solidworks

As shown on the left, the curvature of the saddle surface is very minimal, almost unnoticeable. The image on the right demonstrates the interlocking nature of the male and female saddle sections. The second saddle surface was created in the same manner as the first, except that the assignment of the two radii was reversed. This produced a profile which had a perfect negative profile to the first saddle. Thus, the principal curvatures of the second saddle would be 1/50 in^{-1} (1/1,270 mm^{-1}) and -1/60 in^{-1} (-1/1,524 mm^{-1}).

Once the saddles were designed, they could be 3-D printed using a rapid prototyping machine. The printed test surfaces are shown in the following figure (Figure 21).

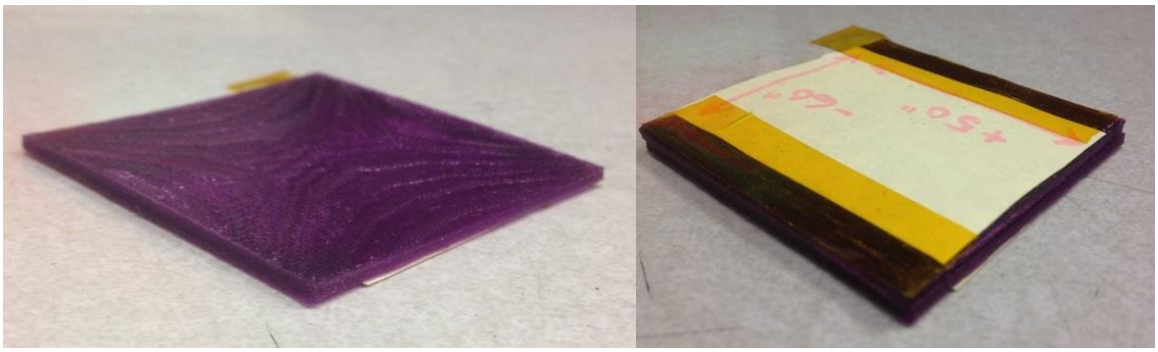

Figure 21: 3-D Printed Saddle Surfaces

Just as in (Figure 20), the figure above shows a single saddle curve as well as the interlocking pair. A side-by-side comparison of the two printed saddle pieces is shown below (Figure 22).

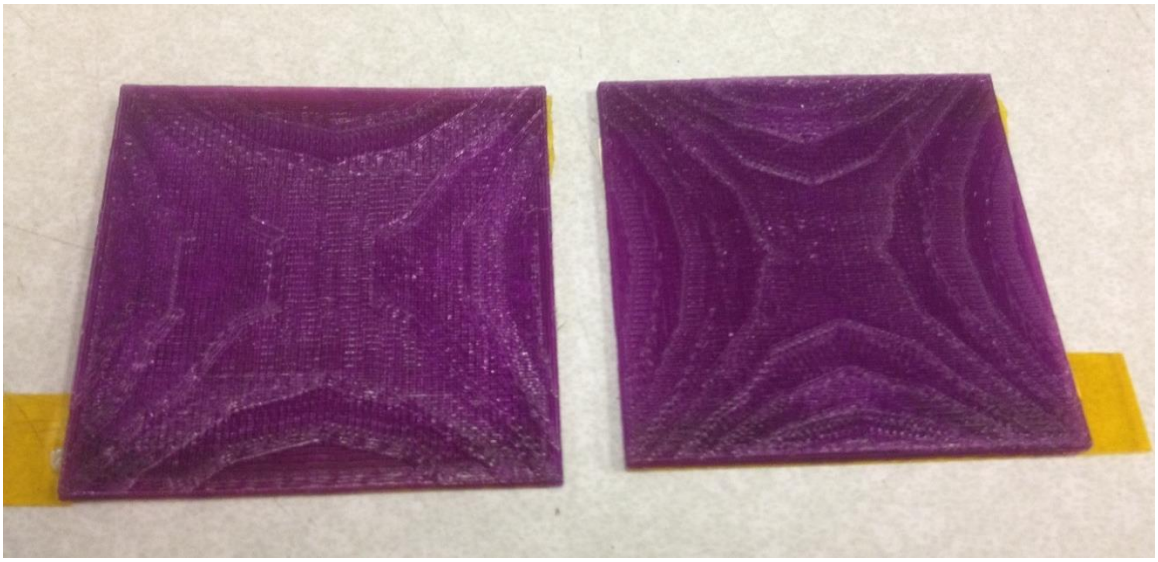

Figure 22: Male and Female Saddle Surfaces

The lines on the two surfaces above are characteristic of the fused deposition modeling (FDM) style of 3-D printing. The printed part is essentially built in layers, meaning that the continuous curves in the virtual design will be printed out as discretized sections which attempt to approximate a curve. The implications of this will be further explored in Section 3.2.3.

With the saddles printed, the testing of the CSR could begin. The rosette was initially placed on a flat surface and pressed down with the acquisition software running so that an initial wavelength could be found for each reflected peak which corresponded to the absence of curvature. Then the CSR was placed on the male test saddle surface, as shown below (Figure 23).

Figure 23: The CSR on the Male Test Saddle

Note that the two perpendicular axes of the CSR have been aligned with the principal curvature directions of the test saddle. The third direction runs straight through the center of the saddle, in which direction the expected curvature would be extremely minimal. Next, the female saddle piece was placed on the CSR and carefully aligned to the male saddle surface. This was done using tabs of Kapton tape that had been applied to the printed saddle pieces for exactly this reason. The following figure shows the CSR between the two saddles (Figure 24).

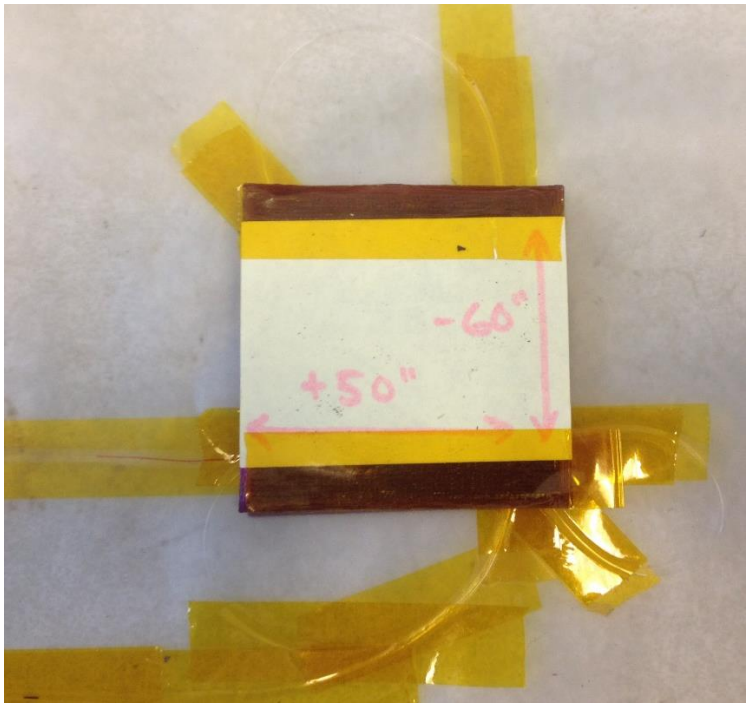

Figure 24: CSR and Saddle Pair Assembly

The top saddle piece was then pressed downwards in order to force the CSR patch to conform to the shape of the two saddles. The entire CSR and saddle pair assembly was

pressed down and subsequently released several times during the test. The figure below shows the window of the data acquisition software during this time (Figure 25).

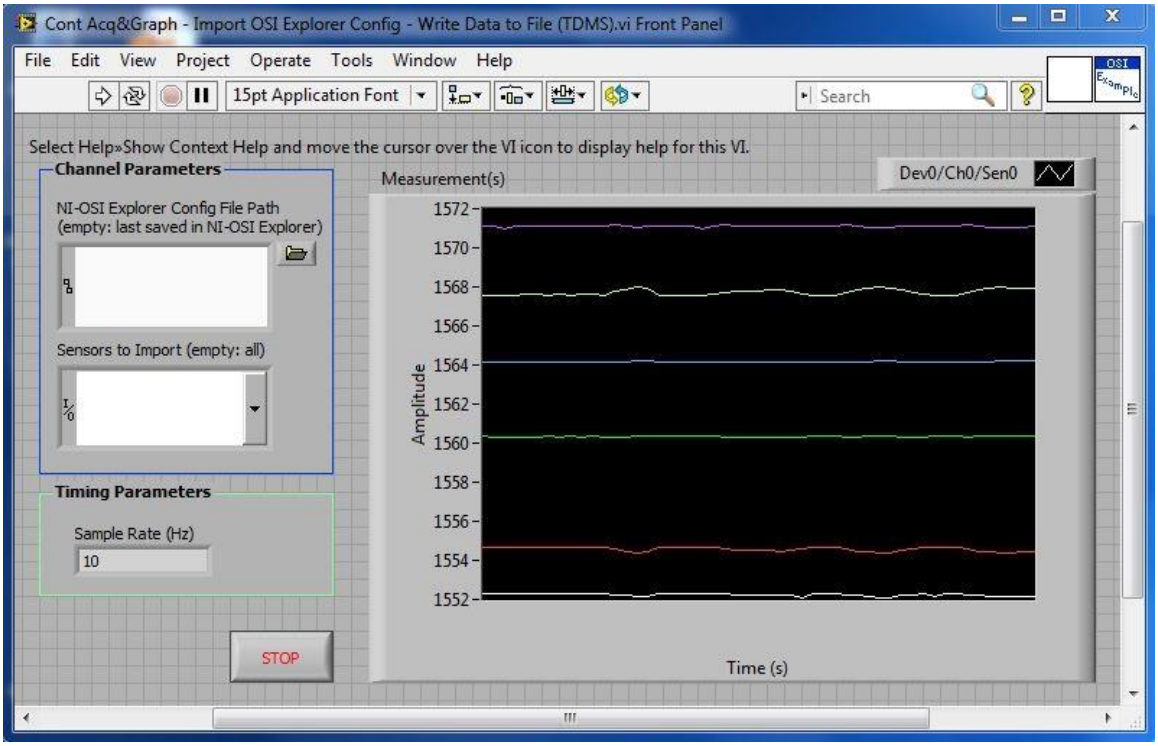

Figure 25: Data Acquisition for the CSR Test

The data were then saved for subsequent analysis. The results of the preceding test are presented in the next section.

3.3.3. Results and Discussion

The CSR test data were analyzed in the same manner as the initial bending test, except of course that two additional curvatures were calculated. From a qualitative standpoint, the test was a complete success; the three curvatures measured by the CSR are all of the appropriate sign and order of magnitude. However, the extremely high accuracy

of the single FBG bend test was not present in the CSR test. There are a number of factors that likely contributed to this inaccuracy, and many of these can be overcome.

The data acquired in (Figure 25) were inspected for usable measurements. Despite the efforts made to ensure that all six of the sensors remained configured throughout the test, there were still some instances in which one or more sensors' data were not collected. This is due in part to the aforementioned issue of configured sensors, but also due to the occasional presence of multiple peaks. The single peak of an FBG can become noisy after encountering too many tight bends in the fiber optic cable. This is because a tight bend essentially increases the angle of internal reflection required for a light signal to remain within the fiber. This can cause the original light to be dispersed as a portion of it escapes the fiber or gets scattered. This results in the presence of multiple peaks showing up within the predefined range of a single peak, which causes the sensor within that range to be in a so-called error state. Just as when a sensor is unconfigured, this results in no data being collected for a sensor while it is in a state of error.

Out of the several instances when the saddle assembly was pressed to give the CSR the same shape as the saddles, only one trial yielded measured values for all six sensors. The following figure shows a graph of this successful trial, and an example of a trial which was ultimately not used due to one or more sensors being in error state (Figure 26).

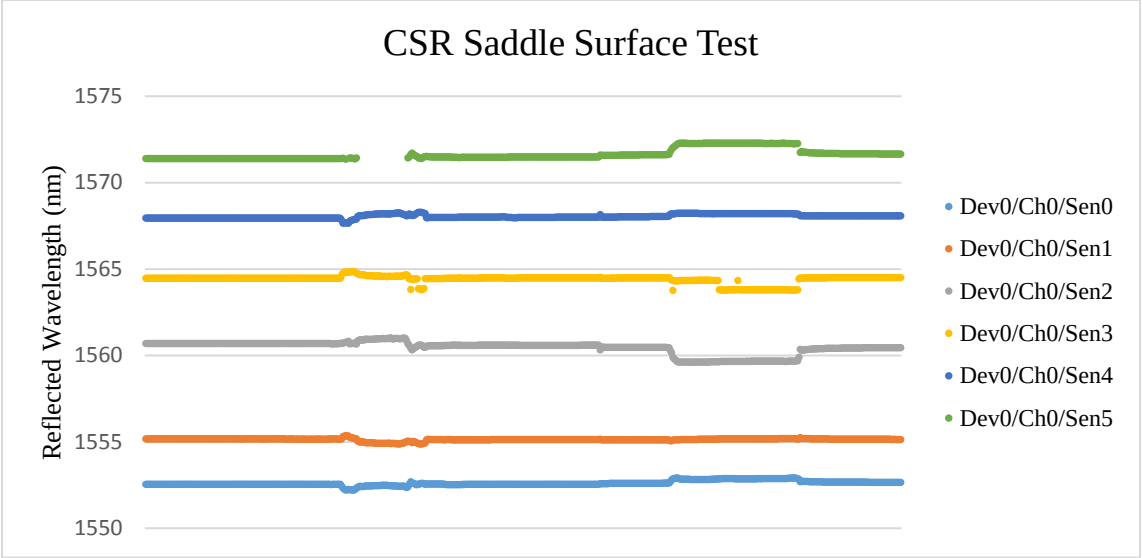

Figure 26: Sample Data from the CSR Saddle Test

Note how on the far left, all sensors are present and apparently reading constant curvature. This corresponds to the time when the CSR was initially pressed into a flat configuration. Moving to the right, there is a point at which the top-most sensor disappears from the graph. This is actually during the process of removing the CSR from the flat surface and onto the male saddle piece. The CSR patch was unintentionally bent through a relatively extreme curve during this transition. The missing sensor, which has the highest wavelength, is the sensor which is furthest from the interrogating light source. This light must therefore pass through the most loops before reaching this FBG, which is why this sensor is shown to be in error state. Once the CSR is placed in the saddle assembly, the missing sensor returns and all six FBGs seem to level off. That is until the saddle pieces are pressed together for a time, then released once more. This describes the phenomenon to the left of the graph. Note how some sensors show a positive shift, while others indicate a negative shift in wavelength. Just as with the simple bend test, the positive values correspond to the FBGs

in tension whereas the negative shifts correspond to FBGs in compression. Once more, their measured peak values, as well as their calculated strains, are tabulated below (Table 3).

Table 3: CSR Saddle Test Data

Sensor	λ_o (nm)	λ (nm)	ε
0	1552.149	1551.726	-0.000349
1	1555.355	1555.500	0.000120
2	1559.830	1560.649	0.000673
3	1564.356	1564.744	0.000318
4	1567.842	1567.815	-0.000022
5	1571.776	1571.354	-0.000344

As expected, three of the calculated strains are positive and three are negative. Due to the layout of the FBG pairs, and immediate qualitative understanding of the surface can be inferred. Refer to the following schematic diagram of the CSR for clarification (Figure 27).

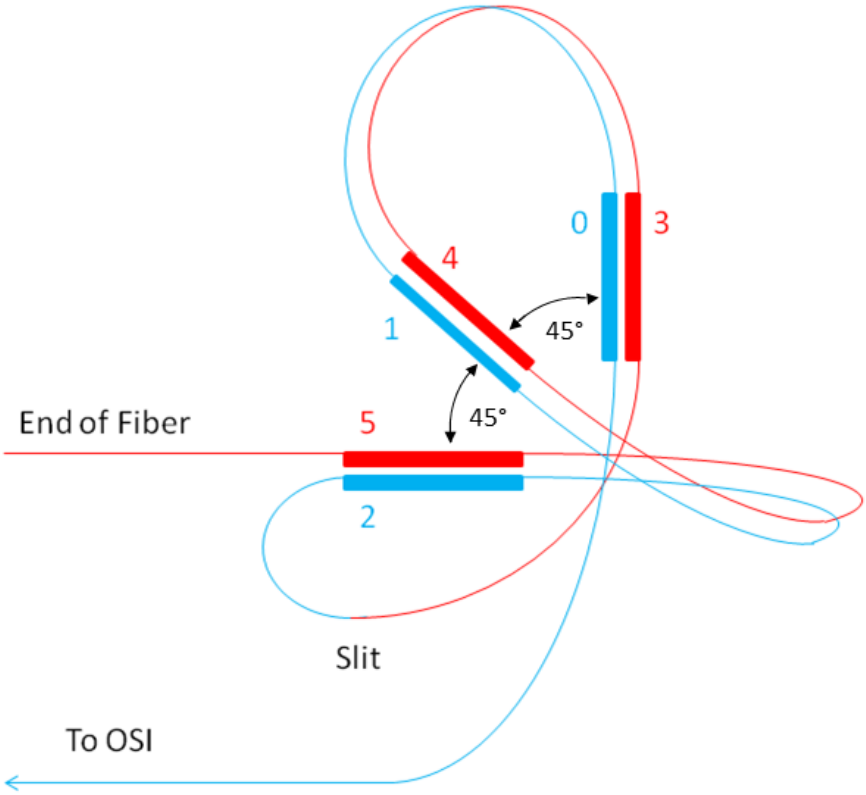

Figure 27: CSR Schematic Diagram

Note that the blue section of the fiber represents the portion on the top of the patch material; the red represents the portion on the bottom. The thicker rectangular objects represent the FBGs. The location of the slit in the patch material is labeled. This is where the fiber passes through the material. Notice that the pairs are as follows: sensors 0 and 3, sensors 1 and 4, and sensors 2 and 5. The three sensors numbered from 0 to 2 are on the top of the patch, and the sensors numbered from 3 to 5 are on the bottom. By looking at the strain values in Table 3, it can be seen that the curvature is negative in the direction aligned with sensor 0, which is a principal curvature direction, and positive for the other two directions.

This is a simple qualitative check of the CSR, and it is consistent with the expected saddle geometry. The quantitative results are listed in the table below (Table 4).

Table 4: CSR Saddle Test Results

Sensor Pair	$\Delta\varepsilon$	κ_{exp} (mm^{-1})	κ_{act} (mm^{-1})	Accuracy (%)
0 and 3	-0.000667	-0.001876	-0.000656	34.96
1 and 4	0.000142	0.000398	0.000066	16.48
2 and 5	0.001017	0.002861	0.000787	27.52

First, it should be noted that the FBG pair consisting of sensors 1 and 4 was directed between the principal curvature directions. Using the theoretical eigenvalues for the two principal curvatures, the κ_{act} table entry for the central FBG pair was calculated. The fact that the measured curvature is far less than that of the principal directions is again consistent with the saddle geometry of the test surface. For the other two pairs, which align with the principal directions, the sign and relative magnitudes of the measured curvatures are also fairly consistent. However, the accuracy of each measured curvature when compared to its true or actual value is far from ideal. Given that they were all much smaller than expected, it was believed that the separation distance between the sensors was in fact greater than originally thought.

Recall again the equation (10) from Section 2.2.1 which gives a curvature reading based on two FBG strain sensors. The difference in strain is divided by the separation distance, which in this case was the thickness of the patch material. Although the thickness of a sample portion of the patch material was measured prior to the construction of the CSR, it is likely that the final thickness of the material between the sensor pairs differed

from the initial measurement. Not only is the patch itself likely to vary in thickness due to manufacturing tolerances, but any amount of excess adhesive could build up and contribute to the overall thickness. To put this in perspective, the initial thickness of the patch was measured via optical comparator and found to be 356 μm. This is barely larger than a third of a millimeter. If a similar thickness of adhesive was deposited on each side of the patch, then the total patch thickness would increase by a factor of three. This is roughly the factor by which the measured principal curvatures differ from their expected actual values.

Given that the accuracy of this FBG curvatures sensing method was demonstrated during the simpler bend test, this unknown thickness increase is likely the cause of the inaccuracy of the CSR test results. It should be noted that the bend test results were not affected in the same manner because the thickness of the test specimen itself was several orders of magnitude greater than the supposed added thickness of the adhesive. For the CSR Saddle test, the fact that the values of the inaccuracies of the principal curvatures vary between themselves would indicate that the unknown combined thickness of the patch and adhesive is itself variable. The fact that the central FBG pair shows the greatest discrepancy is likely due to a combined error due to unknown separation distance and test surface quality. The characteristic layers of the FDM rapid prototyping process can be plainly seen in (Figure 22). Because this direction theoretically had the least amount of curvature by an order of magnitude, any surface inconsistencies would be greatly reflected by the overall accuracy of this FBG pair.

Assuming that the FBG method itself was accurate, the actual curvature values were used to solve for the true separation distances, thereby attempting to calibrate the CSR.

The new thickness of the materials between sensors 0 and 3 was found to have increased by a factor of 2.86, while the thickness between sensors 2 and 5 had increased by a factor of 3.63. These resulted in thicknesses of 1.0 mm and 1.3 mm, respectively. Again, this seems to be a plausible thickness for both patch material and adhesive. The central FBG separation distance was calibrated to be 2.16 mm; however, this may or may not be accurate depending on the error in the test surface in this direction.

The apparent variability of the true thickness of the material between sensor pairs make for a difficult summary of the overall accuracy of the CSR. Any statement regarding its accuracy would necessarily be made with caveats. That being said, the success of the Saddle test from a qualitative standpoint does indicate that the CSR has the potential to be more accurate, provided some adjustments are made. These are necessary improvements for making the CSR a viable option for measuring the curvature of a surface. Once implemented, these alterations could make the CSR the preferred curvature sensor for next-generation inflatable shape sensing systems.

First and foremost, the issue of the excess deposition of the cyanoacrylate adhesive must be addressed. This is the main cause of the inaccuracy of the CSR, and solving this issue would likely remove the need for calibrating the CSR in the directions of principal curvature. Fortunately, there are several methods listed in [22] which can improve the consistency with which the adhesive is applied. One such method involves using a glass form to hold the fiber in place while gluing it to the patch material. Another technique requires the use of Kapton tape to secure the FBG while a low-viscosity adhesive is vacuum-pumped along the length of the fiber. This allows the adhesive to fill any gaps

between the Kapton and the patch material [22]. Finally, a number of thermoplastic resins could be used in place of the cyanoacrylate adhesive. These would require forms to be placed over the FBGs while the resin is poured and cured. In general, any deliberate method for attaching the fiber to the patch material in a consistent manner could be utilized with great effect.

The next major area for improvement of the CSR is the configuration of the multiplexed FBG chain which contains the important stain sensors. As stated, the particular multiplexed fiber that was used in this investigation was less than ideal. This was a result of nothing more than a learning curve associated with purchasing multiplexed FBG chains. The specific fiber used here was ordered with the intent of obtaining a large number of sensors in a single fiber. Because of the lead times associated with ordering a custom multiplexed FBG chain, the final design of the CSR was not yet known at the time of the purchase. The required functionality of the fiber chain was pure conjecture when it was ordered. Had the CSR design been finalized, the FBG chain could have been made to contain only six FBGs. For the same range of 1,510 to 1,590 nm, this would greatly increase the separation of the wavelengths associated with each FBG. This means that when configuring the software to detect each peak, a much wider range could be listed in which to find said peak. This in turn would allow the CSR to remain functional over surfaces with higher curvature magnitudes than the specially designed test surface. Additionally, the physical spacing of the FBGs along the fiber could have been increased significantly. This would mean that more fiber length could be used to make the same turns that were necessary to align the FBG pairs with the predefined axes of curvature

measurement. The result would be a much greater bend radius of the fiber in between FBGs, which would reduce the loss of signal and multiple peaks caused by excessive bending in the fiber. Finally, six individual fibers could be used to produce the same FBG layout required by the CSR. However, this would require a fiber *bundle* to reach the CSR as opposed to a single fiber. This can potentially be quite arduous, considering the number of CSRs that would likely be needed to sense the shape of a space inflatable. As it stands, several CSRs could be made on a single multiplexed fiber, which would likely more useful to any potential shape sensing system. Another alternative is to create a network of multiplexed fibers to produce an array of CSRs, shown in the figure below (Figure 28).

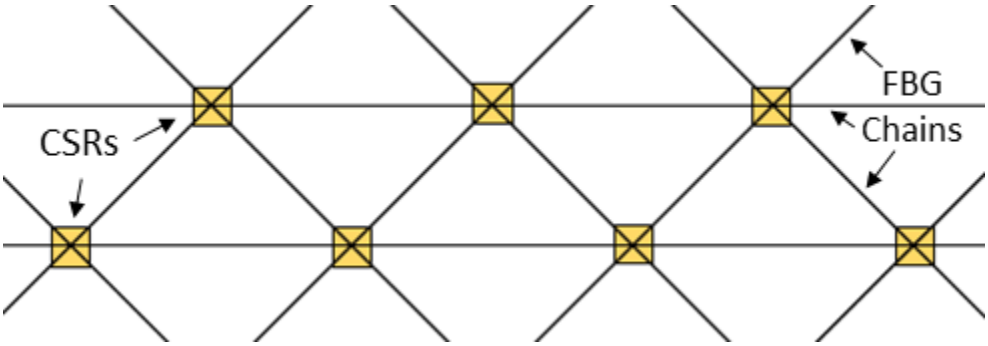

Figure 28: Proposed CSR array

The configuration shown in the figure above could be implemented on an inflatable surface, with three FBGs forming a CSR at each intersection.

The final area for improving the results of the CSR saddle test is in the making of the test surface itself. While the virtual designs of the two saddle surfaces were ideal, the physical printed part was flawed. This is due to the FDM style of rapid prototyping, which deposits layers of molten plastic from a heated nozzle. This causes every piece printed this

way to have a surface texture, as well as discretized curves. There are several methods described in [23, 24] which could greatly reduce these effects, making the saddle pieces much smoother. Additionally, the resolution of the pieces could have been improved by using a more precise machine. Of course, there is a higher cost associated with these high resolution 3-d printers, and this would need to be considered. Employing either of these strategies could reduce the texture of the test surface itself, thus improving the overall accuracy of the test results.

Assuming that the above changes can be implemented, the accuracy of the CSR could be dramatically improved. This would make it a viable option for sensing the surface curvature of inflatable space structures, or any body for which the geometry must be defined. This is because there are several features inherent to its design which allow the CSR to be tailored for individual applications.

For example, the patch design allows for a simple surface application of the CSR, but a more permanent embedding of the sensor array could be achieved with the same sensor configuration. The patch material itself could be replaced with a more rigid or flexible alternative, depending on the application.

Additionally, the layout of the FBGs could be customized for specific geometries. In the current design, there is actually an offset of roughly one inch between the FBGs themselves and the point at which their axes intersect. This was not an issue for the saddle test, but may be for more irregular geometries. For an intricately detailed body, or a particularly vital section of a body, the sensors could be spaced much more closely together. Conversely, for a large or relatively simple body, the sensors could be spaced

more widely apart. This is true of the spacing of the CSR arrays as well. In fact, all of the customizing options discussed for the bend sensors of the CBIC in Section 2.3.3 are likewise applicable to the CSR. These qualities make the CSR a potentially viable solution for the current need for accurate shape sensors.

CHAPTER 4: CONCLUSIONS

One of the many strides being made in the growing field of space exploration is the use of inflatable structures. These inflatable bodies offer many advantages over traditional, rigid structures, but present some unique challenges as well. Among these is the need for accurate determination of the complete geometry of the body, known as shape sensing. This is an important tool for monitoring both the inflation status and overall health of inflatables. While differential geometry can describe the shape, it cannot be directly measured. Instead, the surface curvature at certain point on a body is measured, and the underlying geometry can be inferred.

This surface curvature exists in two dimensions, yet contemporary methods can only measure one-dimensional curvature. This is the curvature which is characteristic of a space curve, which is a one-dimensional mathematical construct. Although space curves exist in three dimensions, they are subject to curvature in one and only one direction at a time. This means that current techniques for sensing curvature only describe a single space curve and not an entire surface. To circumvent this issue, NASA has developed a multi-core, multiplexed chain of Fiber Bragg Gratings. This device is essentially a self-sensing space curve, which can detect one-dimensional curvature in any direction. These curvature measurements are used in subsequent calculations to produce a virtual image of the FBG chain itself. By overlaying this fiber bundle on an unknown surface, the virtual image will provide a limited depiction of said surface. Alternative methods are required to truly identify the geometry of an unknown surface.

One such alternative is the flex sensor, which is a widely available and highly economic option. However, in addition to being generally less accurate, these one-dimensional curvature sensors suffer from similar pitfalls as the NASA FBG chain. Despite this, their availability and ease of operation made flex sensors the most suitable option for the development of an inflation controller. This controller would use curvature feedback from flex sensors to monitor the inflation of a body and was thus named the Curvature-Based Inflation Controller. The design of the CBIC attempted to overcome the inherent shortcomings of the flex sensors by placing them at strategic points on the inflatable. This allowed the CBIC to correctly sense the completion of the inflation process, and power off the air pump accordingly. This proved the viability of both the CBIC's design and the use of shape sensing as a means of controlling inflation in general. Several features of the CBIC make it a useful design for inflation controllers; most notably, the modularity of its layout and the relatively robust sensors it employed.

While it succeeded in the task of inflating an air mattress using only curvature measurements, the CBIC's limitations were many. The simplicity of its control architecture relied heavily on a predictable and well-behaved inflation process. Additionally, its method of shape determination suffered from the inability of its sensors to measure curvature in more than one direction.

This is a fundamental flaw of every contemporary shape sensing method, because unlike space curves, surfaces extend in two dimensions. Within the two-dimensional surface, there are infinitely many directions along which the curvature can potentially be measured. Despite this, only three unique components are required to develop a metric for

a surface. This metric can then be used to measure arc lengths, angles, and areas on the surface which it defines. The metric tensor can potentially be determined using the principal curvatures and the two fundamental forms of a surface. These principal curvatures and their associated directions are thus extremely important for the purposes of shape determination.

In order to measure the principal curvatures of a surface, a novel sensor array was designed. This Curvature-Sensing Rosette utilized a single multiplexed chain of FBGs to sense curvature in two orthogonal directions and along the 45° angle in between them. These measurements would theoretically allow for the surface geometry of a body to be known. After a preliminary experiment which proved the accuracy of the FBG method of sensing curvature, the proposed CSR was fabricated.

In order to properly test the new sensor array, a custom pair of interlocking saddle surfaces were 3-D printed after being designed in the CAD program Solidworks. Although the surface texture of the saddles produced by the FDM was not ideal, this rapid prototyping was necessary to ensure the production of a surface with controlled saddle geometry. In addition, the two male and female profiles allowed for the CSR to be pressed into conforming exactly to the saddle surface.

The results of the CSR test were mixed; on the whole it was a success, but several glaring issues with the CSR's fabrication led to some rather inaccurate measurements. These flaws were identified as an improper method of fiber adhesion and an inappropriate configuration of the multiplexed FBG chain. Provided these can be addressed in

subsequent iterations, the CSR could prove to be a viable means of sensing curvature in multiple directions at one time.

This is because the CSR succeeded in detecting the signs of the curvatures which it measured, and the accuracy of FBGs in sensing curvature in general is known to be exceptional. Thus, imbuing the CSR with high-accuracy curvature detection is quite plausible. This would allow for the surface geometry of the area surround the CSR to be rigorously defined. By employing a network of CSRs across the total surface of an inflatable body, the complete shape of the inflatable can be known in real time. Such a means of shape sensing would be invaluable to mission controllers seeking to monitor and control the inflation status and overall health of an inflatable space structure.

REFERENCES

[1] R. E. Freeland, G. R. Veal. (1998) "Significance of the Inflatable Antenna Experiment technology." *American Institute of Aeronautics and Astronautics, Inc.*[Online]. 98(2104).

[2] "Inflatable Antenna Experiment (IAE)." Internet: https://www.dvidshub.net/image/743006/inflatable-antenna-experiment-iae, Dec. 15, 2010 [Nov. 8, 2016].

[3] S. J. Hughes *et al*. (2011, May) "Hypersonic Inflatable Aerodynamic Decelerator (HIAD) Technology Development Overview." In *21st AIAA Annual Aerodynamic Decelerator Systems Technology Conference and Seminar*, 2011 [Online].

[4] "Hypersonic Inflatable Aerodynamic Decelerator (HIAD)." Internet: http://www.nasa.gov/offices/oct/game_changing_technology/game_changing_development/HIAD/IMG-hiad-angle.html, July 16, 2012 [Nov. 8 2016].

[5] J. P. Moore, M. D. Rogge. "Shape sensing using multi-core fiber optic cable and parametric curve solutions." *Optics Express*, vol. 20, pp. 2967-2973, Jan. 2012.

[6] M. D. Greenberg. *Foundations of Applied Mathematics*. Mineola, New York: Dover Publications, Inc., 2014, pp. 147-148.

[7] Internet: https://technologygateway.nasa.gov/images/misc/moore-shape-sensing.jpg, [Nov. 8, 2016]

[8] E. Kreyszig. *Differential Geometry*. New York: Dover Publications, Inc., 2015, pp. 72-152.

[9] D. J. Struik. *Lectures on Classical Differential Geometry*. New York: Dover Publications, Inc., 2013, pp. 55-124.

[10] R. Kashyap. *Fiber Bragg Gratings, 2nd Edition*. Massachusetts: Elsevier Inc., 2010, pp. 18-59.

[11] K. O. Hill, G. Meltz. "Fiber Bragg Grating Technology Fundamentals and Overview." *Journal of Lightwave Technology*, vol. 15, pp. 1263-1276, Aug. 1997.

[12] "Working principle of FBG." Internet: http://www.fbgs.com/technology/fbg-principle/, 2016 [Nov. 8 2016].

[13] E. Udd. *Fiber Optic Sensors: An Introduction of Engineers and Scientists*. New York: John Wiley and Sons, Inc., 1991, pp. 9-35, 340-365.

[14] M. Kreuzer. "Strain Measurement with Fiber Bragg Grating Sensors." Internet: http://micronoptics.ru/uploads/library/documents/FBGS_StrainMeasurement_mo.pdf, [Nov. 8, 2016].

[15] "FBG response as function of strain." Internet: http://www.fbgs.com/technology/fbg-principle/, 2016 [Nov. 8, 2016].

[16] G. B. Langford, "Flexible Potentiometer," U.S. Patent 5 583 476, Dec. 10, 1996.

[17] "Sensors: bendshort-alpha." Internet: http://www.sensorwiki.org/lib/exe/detail.php/sensors/bendshort-alpha.png?id=sensors%3Aflexion&cache=cache, Nov. 15, 2011 [Nov. 8, 2016].

[18] Internet: http://arduinosensors.com/wp-content/uploads/2014/08/flexsensor3.png, [Nov. 8, 2016].

[19] M. P. do Carmo. *Differential Geometry of Curves and Surfaces*. Englewood Cliffs, New Jersey: Prentice-Hall, Inc., 1976, pp. 83-153.
[20] J. A. Thorpe. *Elementary Topics in Differential Geometry*. New York: Springer-Verlag, 1979, pp. 53-94.
[21] "Invisible Handshake." Internet: http://stanwagon.com/wagon/misc/htmllinks/invisiblehandshake_3.html, [Nov. 8, 2016].
[22] I. Grabovac, T. Nuyens, C. Davis. (2010, Oct.). "Packaging and Mounting of In-Fibre Bragg Grating Arrays for Structural Health Monitoring of Large Structures." *Defence Science and Technology Organisation*. [Online]. 2490. Available: www.dtic.mil/cgi-bin/GetTRDoc?AD=ADA536063 [Nov. 8, 2016].
[23] A. Boscetto, L. Bottini, F. Veniali. (2016). "Finishing of Fused Deposition Modeling parts by CNC machining." *Robotics and Computer-Integrated Manufacturing*. [Online]. 40, pp. 92-101. Available: http://ac.els-cdn.com/S0736584515300648/1-s2.0-S0736584515300648-main.pdf?_tid=db4e9a06-a593-11e6-bbfa-00000aacb35f&acdnat=1478596694_784c33e1dd743ff47ffa83395e9d06ac [Nov. 8, 2016].
[24] P. M. Pandey, N. V. Reddy, S. G. Dhande. (2002, Sep.). "Improvement of surface finish by staircase machining in fused deposition modeling." *Journal of Materials Processing Technology*. 132, pp 323-331. Available: http://ac.els-cdn.com/S0924013602009536/1-s2.0-S0924013602009536-main.pdf?_tid=d74e9230-a593-11e6-83ef-00000aacb361&acdnat=1478596687_b086958a120eebee99ff326d0285ded0 [Nov. 8, 2016].

APPENDIX

```
/*
Multiple Sensor Relay Code
Takes the analog inputs from 6 sensors and uses
them to turn off a relay on digital pin 13.
 */

const int sensor1Pin = A0;    // select the input pin for the sensor 1
const int sensor2Pin = A1;    // select the input pin for the sensor 2
const int sensor3Pin = A2;    // select the input pin for the sensor 3
const int sensor4Pin = A3;    // select the input pin for the sensor 4
const int sensor10Pin = A4;    // select the input pin for the sensor 10
const int sensor11Pin = A5;    // select the input pin for the sensor 11

const int relayPin = 13;      // select the pin for the relay

int sensor1Value = 0;      // variable to store the value coming from the
                           // sensor 1
int sensor2Value = 0;      // variable to store the value coming from the
                           // sensor 2
int sensor3Value = 0;      // variable to store the value coming from the
                           // sensor 3
int sensor4Value = 0;      // variable to store the value coming from the
                           // sensor 4
int sensor10Value = 0;     // variable to store the value coming from the
                           // sensor 10
int sensor11Value = 0;     // variable to store the value coming from the
                           // sensor 11

void setup() {

  pinMode(relayPin, OUTPUT);      // declare the relayPin as an OUTPUT:

  Serial.begin(9600);           // initialize serial communications at 9600
                                // bps:
}

void loop() {

  sensor1Value = analogRead(sensor1Pin);     // read the values from the
                                             // sensors
  sensor2Value = analogRead(sensor2Pin);
  sensor3Value = analogRead(sensor3Pin);
  sensor4Value = analogRead(sensor4Pin);
  sensor10Value = analogRead(sensor10Pin);
  sensor11Value = analogRead(sensor11Pin);

  if (sensor1Value<300)                   // keep pump turned on until all
    digitalWrite(relayPin, HIGH);         // sensors are reading their
  else if (sensor2Value<320)              // respective threshold values
    digitalWrite(relayPin, HIGH);
  else if (sensor3Value<380)
    digitalWrite(relayPin, HIGH);
  else if (sensor4Value<350)
    digitalWrite(relayPin, HIGH);
  else if (sensor10Value<340)
    digitalWrite(relayPin, HIGH);
  else if (sensor11Value<300)
```

```
    digitalWrite(relayPin, HIGH);
  else
    digitalWrite(relayPin, LOW);

  Serial.print("L1 = ");         // print the results to the serial monitor:
  Serial.print(sensor1Value);
  Serial.print("       L2 = ");
  Serial.print(sensor2Value);
  Serial.print("       L3 = ");
  Serial.print(sensor3Value);
  Serial.print("       L4 = ");
  Serial.print(sensor4Value);
  Serial.print("       L10 = ");
  Serial.print(sensor10Value);
  Serial.print("       L11 = ");
  Serial.println(sensor11Value);


  delay(2000);                     // wait 2 seconds before the next loop
}
```